UNIVERSITAT POLITÈCNICA DE CATALUNYA
BARCELONATECH

Numerical resolution of heat and mass transfer phenomena. Application to the estimation of heat and mass transfer coefficients in absorption processes with falling film

Master of Energy Engineering

MSc Thesis

AUTOR: JIAN ZHENG

SUPERVISOR: JESUS CASTRO GONZALEZ

COMMOTEE MEMBERS:

PRESIDENT	CARLOS DAVID PÉREZ SEGARRA
VOCAL	JESUS CASTRO GONZALEZ
VOCAL	CESAR ALBERTO VALDERRAMA
VOCAL SUBSTITUTE	ENRIQUE VELO GARCIA
VOCAL SUBSTITUTE	IGNASI CASAS PONS

DATE 09/2017

Acknowledgement

Firstly, I would like to thank the director of my project prof. Assensi Oliva and CTTC group for having provided me the opportunity to study in the laboratory and work with many enthusiastic colleagues. Also, I should say thanks to Jordi Chiva and Arnau Pont for the generous support at programming skills, with which I acquired a full comprehension of heat and mass transfer phenomena.

In the experiment part, I would like to say thanks to prof. Jeus Catro Gonzalez and Nicolas Valle Marchante for having provided the opportunity of taking part in the experiment of absorption chiller and working together, in which I have learned a lot in maintaining vacuum system and mechanical skills. Meantime, thank Joan Farnos for helping me understand the absorption working system and his machine.

Finally, special thanks to my family especially my father for their unconditionally support and understand.

Abstract

In this project, self-build CFD code in C++ is employed to simulate several classical fluid dynamic, heat and mass transfer problems such as Driven Cavity, Deferential Heat Cavity, Square Cylinder problem. Besides, this work also includes a code of absorption chiller in condition of falling film, and the result of the code will be compared with previous work of other researchers.

The inform consists of 6 chapters. Chapter 1 is introduction where the objective and scope is explained. In chapter 2, the govern equation of both mass, momentum and energy equation will be deduced at different conditions using different hypothesis and simplification. In chapter 3, the discretization of the govern equation and the mesh of the domain will be carried out. In chapter 4, the algorithm of fractional method step will be explained and, also the algorithm for the falling film. In chapter 5, the result of each corresponding code will be compared with high resolution benchmark result. In the final chapter 6, an experiment of component of absorption chiller with falling film of aqueous LiBr driven by gravity is carried out. The experiment should be operated in vacuum condition at absolute pressure around 1000 Pa, but no experiment data is acquired due to the lack of time. The information of experiment apparatus will be demonstrated in the annex.

Table of Contents

Table of Contents

List of figures

List of figures

List of tables

Nomenclature

a	Acceleration	B	Block ratio
C	Concentration of solution	C_p	Specific heat capacity
C_d	Drag force coefficient	C_l	Lift force coefficient
D	Species diffusivity	e	Energy
F	Surface force	f	Mass force
g	Gravity	P_v	Vapor pressure
h	Convection heat transfer coefficient	S	Source term
J	Diffusion flux	L,l	Length, m
$\dot{m}$	mass flow rate	m	Mass, kg
p	Pressure	q	Heat flux
S	Surface extension	T	Temperature
t	Time	u	Velocity of x coordinate
V	Volumen	v	Velocity of y coordinate
x	x coordinate	y	y coordinate
z	z coordinate		

Greek symbols

α	Thermal diffusivity	β	Thermal expansion coefficient
ε	Error	ϕ	Dimensionless transport variable
λ	Thermal conductivity	μ	Dynamic viscosity
ν	Kinetic viscosity	θ	Inclination angle, rad
ρ	Density	σ	General force
τ	Shear force	Φ	Heat source
ψ	Value of streamline function	Ω	Calculate domain

Dimensionless groups

Re	Reynolds number	Ra	Raleigh number
Pr	Prandtl number	Nu	Nusselt number
St	Strouhal number		

Subscripts

abs	absorption	b	bulk
c	coolant fluid	eq	equilibrium condition
in	inlet condition	out	outlet condition
s	solution	v	vapor
w	solid wall		

Superscripts

–	Normaliza	n	Current time step
p	Predicted	*	Dimensionless
$\rightarrow$	Vector		

Chapter 1: Introduction

1.1 Objective

CFD is now an essential instrument in both industry and academia area, since it is a powerful tool that enables companies to test their product with low expenses compared to the expansive experiments or researchers to predicate physical phenomena or PDEs resolution. Besides, implementation of self-built CFD code could give better understanding of Navier-stokes equation and many physical phenomena.

In this project, self-built CFD code written in C++ is used to simulate Driven Cavity, Deferential Heat Cavity, Square Cylinder and LiBr solution with falling film. The numerical result of the heat and mass performance of falling film will be compared to the result of previous work while the rest will be compared to the benchmark solution. And an experiment unit is installed to investigate the heat and mass transfer performance of falling film. Due to the lack of time, only basic test experiment data was acquired.

1.2 Scope

The following highlights are aggressed in this work:

- Incompressible Navier Stokes equation is solved with some simplifying hypothesis
- Heat and mass transfer performance of 2D fluid will be researched
- Details like flow pattern, vertex shedding, streamline function, temperature, pressure, and velocity distribution is demonstrated in the result
- Heat and mass transfer performance of falling film of LiBr solution is revealed with numerical solution
- An experiment apparatus is set up to study the falling film problem

Chapter 2: Governing equation

2.1 Introduction

In this chapter, the governing equation in the domain will be demonstrated and also the relative functions. The governing equation contains the mass and momentum equation in the domain. In order to simplify the calculation area, hypothesis as below are considered.

- Incompressible flow
- Dimensional flow
- Newton fluid
- Radiation negelected
- Physic properties constant
- Boussinesq approximation in term of nature convection

2.2 Mass equation

2.2.1 Mass conservation

The principle of continuity conservation is the first should be considered when deal with an open system element. A simple model of 2D element in an open system is presented as Fig 2.2.1, by applying physical principle to the control volume, it could be obtained as an expression that the net flow leaves a control volume equal to the temporal decrement of mass.

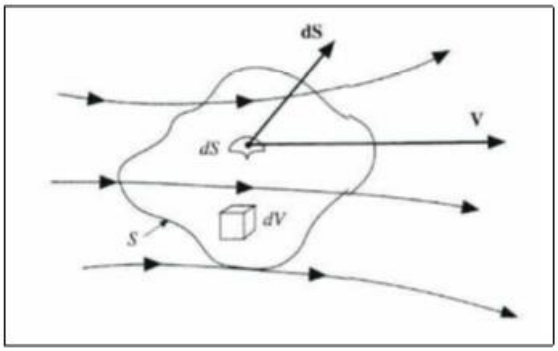

Fig 2.2.1 Control volume in the flow path

Within mathematic formulation, the expression above could be transmitted as equation below:

$$\text{Mass Flow} = \rho V \mathrm{d}S \tag{2-1}$$

$$\text{Net Leave Mass} = \int_S \rho \vec{v} \cdot \vec{n} \mathrm{d}S \tag{2-2}$$

$$\text{Mass in the control volume} = \int_V \rho \mathrm{d}V \tag{2-3}$$

$$\text{Temporary decrement of mass} = -\frac{\partial}{\partial t} \int_V \rho \mathrm{d}V \tag{2-4}$$

Finally, the integral form of continuity equation which represents the net mass leaves the control volume equal to internal mass decrement could be obtained as below:

$$\frac{\partial}{\partial t} \int_V \rho \mathrm{d}V + \int_S \rho \vec{v} \cdot \vec{n} \mathrm{d}S = 0 \tag{2-5}$$

2.2.2 Differential form for continuity equation

Continuity equation (2-5) could be expressed in a differential form, which is as showed below eq. (2-6),

$$\frac{\partial \rho}{\partial t} + \nabla \cdot (\rho \boldsymbol{u}) = 0 \tag{2-6}$$

when the fluid is incompressible, the equation is (2-7)

$$\frac{\partial u}{\partial x} + \frac{\partial v}{\partial y} = 0 \tag{2-7}$$

2.3 Momentum equation

2.3.1 General force on the control volume

The conservation of momentum could be deducted from the Newton second law, which means the acceleration of an object as produced by a net force is directly proportional to the magnitude of the net force, in the same direction as the net force, and inversely proportional to the mass of the object, in a corresponding coordinate could be expressed as:

$$F_x = m a_x \tag{2-8}$$

In another way, the integral equation could be obtained in a control volume as[1]:

$$\frac{\partial}{\partial t}\int_V \vec{v}\cdot\vec{n}\rho \mathrm{d}V + \int_S \vec{v}\rho\vec{v}\cdot\vec{n}\mathrm{d}S = \int_S f_{(\vec{n})}\rho \mathrm{d}V + \int_V \vec{g}\cdot\vec{n}\rho \mathrm{d}V \tag{2-9}$$

In which, $\frac{\partial}{\partial t}\int_V \vec{v}\rho \mathrm{d}V$ this integral term represents the decrement temporary momentum inside the control volume.

$\int_S \vec{v}\rho\vec{v}\cdot \mathrm{d}S$ means the integration of momentum change through the surface of the control volume.

$\int_S f_{(\vec{n})}\rho \mathrm{d}V$ represents surface forces, the distribution of tangent tensions and normal action on the surface of the control volume by direct contact.

$\int_V \vec{g}\rho \mathrm{d}V$ represents basic forces, which impact directly on the volumetric mass of the fluid element with no direct contact. Basics forces could be electrical, gravitational, magnetic or others.

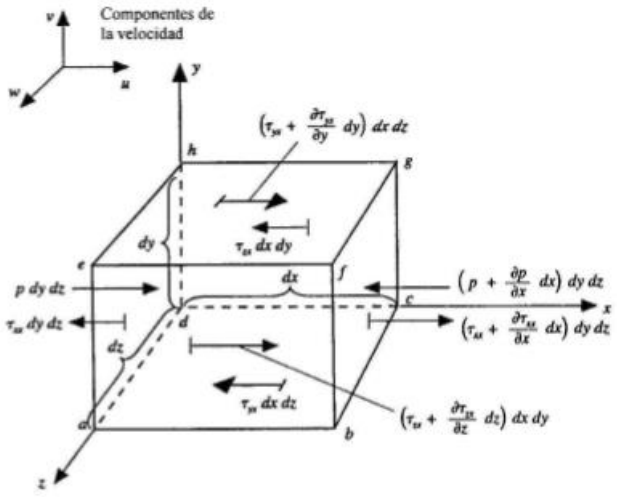

Fig 2.2.2 Motion of moving element in *x* direction

2.3.2 Surface force

For further expression, surface forces f_x and mass force F_{mass} could be deducted as:

$$F_{mass} = \rho f_x(\mathrm{d}x\cdot \mathrm{d}y\cdot \mathrm{d}z) \tag{2-10}$$

According to the Lagrange-d'Alemebert principle, the force and force moment should maintain balanced. On the specific element like Fig 2.2.3, the force weight could be transmitted as:

$$\begin{pmatrix} \sigma_{xx} & \tau_{xy} & \tau_{xz} \\ \tau_{yx} & \sigma_{yy} & \tau_{yz} \\ \tau_{yz} & \tau_{zy} & \sigma_{zz} \end{pmatrix} \tag{2-10}$$

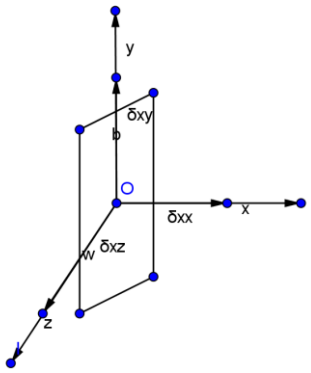

Fig 2.3.1 Element on the cartesian coordinate

Where σ means the general force and τ is viscous force, the footprint means the origin and destination of the force. For axial *z*, it could be deducted that:

$$\begin{aligned} &(\tau_{xy} + \frac{\partial \tau_{xy}}{\partial x}\frac{\delta x}{2})\delta y \delta z \frac{\delta x}{2} + (\tau_{xy} - \frac{\partial \tau_{xy}}{\partial x}\frac{\delta x}{2})\delta y \delta z \frac{\delta x}{2} \\ &= (\tau_{yx} + \frac{\partial \tau_{yx}}{\partial y}\frac{\delta y}{2})\delta x \delta z \frac{\delta y}{2} + (\tau_{yx} - \frac{\partial \tau_{yx}}{\partial y}\frac{\delta y}{2})\delta y \delta z \frac{\delta y}{2} \end{aligned} \tag{2-11}$$

The equation (2-11) will lead to:

$$\tau_{xy} = \tau_{yx} \tag{2-12}$$

According to Newton's fractional law, the viscous force could be expressed as:

$$\tau = \mu \frac{\mathrm{d}u}{\mathrm{d}y} \tag{2-13}$$

In corresponding coordinate of 2D case, the viscous force could be obtained as:

$$\tau_{xy} = \tau_{yx} = \mu(\frac{\partial u}{\partial y} + \frac{\partial v}{\partial x}) \tag{2-14}$$

$$\tau_{xx} = 2\mu\frac{\partial u}{\partial x} - \frac{2}{3}\mu\nabla\cdot\mathbf{V}$$
$$\tau_{yy} = 2\mu\frac{\partial u}{\partial y} - \frac{2}{3}\mu\nabla\cdot\mathbf{V} \quad (2\text{-}15)$$

Where μ is the dynamic viscosity of the fluid, and $\frac{2}{3}\mu\nabla\cdot\mathbf{V}$ is relative volumetric expansion rate which in incompressible flow $\nabla\cdot\mathbf{V}=0$, hence $\tau_{xx} = 2\mu\frac{\partial u}{\partial x}$. As showed in Fig 2.2.2, the arithmetic summation of surface force on an axis could be obtained as:

$$f_{sx} = (\frac{\partial \tau_{xx}}{\partial x} + \frac{\partial \tau_{yx}}{\partial y}) \quad (2\text{-}16)$$

With equation (2-14) and (2-15), (2-16) could also be expressed as:

$$f_{sx} = \mu(\frac{\partial^2 u}{\partial x^2} + \frac{\partial^2 u}{\partial y^2}) + \mu\frac{\partial}{\partial x}(\frac{\partial u}{\partial x} + \frac{\partial v}{\partial y}) \quad (2\text{-}17)$$

In incompressible flow is:

$$f_{sx} = \mu(\frac{\partial^2 u}{\partial x^2} + \frac{\partial^2 u}{\partial y^2}) \text{ or } f_{sx} = \mu\nabla^2 u \quad (2\text{-}18)$$

2.3.3 Mass force

For the conservative formation, we could obtain:

$$\rho\frac{Du}{Dt} = \rho\frac{\partial u}{\partial t} + \rho V\nabla u \quad (2\text{-}19)$$

And could be obtained as:

$$\rho\frac{Du}{Dt} = \frac{\partial \rho u}{\partial t} + \nabla(\rho u V) \quad (2\text{-}20)$$

2.3.4 N-S equation

The equation that describes the motion of viscous fluid substances is known as N-S equations which arise from applying Newton's second law to fluid motion. The momentum equations in a general form is as (2-21) according to (2-20) (2-18), in Cartesian coordinate correspond to (2-22) and (2-23), and in (2-23) Boussinesq approximation is employed.

$$\rho(\frac{\partial v}{\partial t}+(v\cdot\nabla)v)=-\nabla p+\nabla\bar{\tau}+\rho g \tag{2-21}$$

$$\frac{\partial u}{\partial t}+u\frac{\partial u}{\partial x}+v\frac{\partial u}{\partial y}=-\frac{1}{\rho}\frac{\partial p}{\partial x}+\upsilon(\frac{\partial^2 u}{\partial x^2}+\frac{\partial^2 u}{\partial y^2}) \tag{2-22}$$

$$\frac{\partial v}{\partial t}+u\frac{\partial v}{\partial x}+v\frac{\partial v}{\partial y}=-\frac{1}{\rho}\frac{\partial p}{\partial y}+\upsilon(\frac{\partial^2 v}{\partial x^2}+\frac{\partial^2 v}{\partial y^2})+\rho_0\beta(T-T_0)g \tag{2-23}$$

also, the dimensionless forms are (2-24) and (2-25) for the incompressible viscous flow,

$$\frac{\partial u^*}{\partial t^*}+u^*\frac{\partial u^*}{\partial x^*}+v^*\frac{\partial u^*}{\partial y^*}=-\frac{\partial p^*}{\partial x^*}+\frac{1}{Re}(\frac{\partial^2 u^*}{\partial x^{*2}}+\frac{\partial^2 u^*}{\partial y^{*2}}) \tag{2-24}$$

$$\frac{\partial v^*}{\partial t^*}+u^*\frac{\partial v^*}{\partial x^*}+v^*\frac{\partial v^*}{\partial y^*}=-\frac{\partial p^*}{\partial y^*}+\frac{1}{Re}(\frac{\partial^2 v^*}{\partial x^{*2}}+\frac{\partial^2 v^*}{\partial y^{*2}}) \tag{2-25}$$

where $u^*=u/U \quad v^*=v/U \quad x^*=x/L \quad y^*=y/L \quad t^*=t/(U/L)$ $p^*=p/(\rho U^2) \quad Re=\frac{\rho UL}{\mu}$, L is the characteristic length, u and v correspond to the velocity on the x and y axis, p is the pressure, t is time and Re is Reynolds number, μ and υ are dynamic viscosity and kinetic viscosity, $\mu = \upsilon \cdot \rho$.

For the natural convection case, the governing equation will change due to the gravity with Boussinesq approximation, as (2-26) and (2-27).

$$\frac{\partial u^*}{\partial t^*}+u^*\frac{\partial u^*}{\partial x^*}+v^*\frac{\partial u^*}{\partial y^*}=-\frac{\partial p^*}{\partial x^*}+Pr(\frac{\partial^2 u^*}{\partial x^{*2}}+\frac{\partial^2 u^*}{\partial y^{*2}}) \tag{2-26}$$

$$\frac{\partial u^*}{\partial t^*}+u^*\frac{\partial u^*}{\partial x^*}+v^*\frac{\partial u^*}{\partial y^*}=-\frac{\partial p^*}{\partial x^*}+Pr(\frac{\partial^2 u^*}{\partial x^{*2}}+\frac{\partial^2 u^*}{\partial y^{*2}})+Ra*Pr*\vartheta^* \tag{2-27}$$

where $u^*=u/U \quad v^*=v/U \quad x^*=x/L \quad y^*=y/L \quad t^*=t/(L/U)$ $p^*=p/(\rho U^2) \quad Pr=\frac{\mu C_p}{\lambda} \quad Ra=\frac{g\beta(T_s-T_\infty)x^3}{\upsilon\alpha} \quad \alpha=\frac{\lambda}{\rho C_p} \quad \vartheta^*=\frac{T-T_\infty}{T_0-T_\infty}$, Pr is Prandtl number, Ra is Rayleigh number, β is thermal expansion coefficient, α is thermal diffusivity, λ is thermal conductivity.

2.4 Energy equation

2.4.1 General energy equation

equation (2-28) shows the conservation of energy in integral form[3]:

$$\begin{aligned}&\frac{\partial}{\partial t}\int_V (u+e_c)\rho \mathrm{d}V + \int_S (u+e_c)\rho \vec{v}\vec{n}\mathrm{d}V = \\ &-\int_S \vec{q}\vec{n}dS + \int_S \vec{v}\vec{f}\vec{n}\mathrm{d}S + \int_V \vec{v}\vec{g}\rho \mathrm{d}V\end{aligned} \tag{2-28}$$

After integration the equation could be obtained as:

$$\frac{D(u+e_c)}{Dt} = \nabla(\lambda \cdot \nabla T) - P\cdot\nabla\vec{v} + \vec{\tau}:\nabla\vec{v} + \rho\vec{g}\vec{v} \tag{2-29}$$

With the hypothesis of incompressible flow, dimensional flow, Newton fluid, radiation neglectable, physic properties constant, the equation is (2-30), the dimensionless is (2-31)

$$\rho\frac{\partial T}{\partial t} + \rho u\frac{\partial T}{\partial x} + \rho v\frac{\partial T}{\partial y} = \frac{\lambda}{C_p}\left(\frac{\partial^2 T}{\partial x^2} + \frac{\partial^2 T}{\partial y^2}\right) + \frac{\Phi}{C_p} \tag{2-30}$$

$$\frac{\partial T^*}{\partial t^*} + u^*\frac{\partial T^*}{\partial x^*} + v^*\frac{\partial T^*}{\partial y^*} = \alpha\left(\frac{\partial^2 T^*}{\partial x^{*2}} + \frac{\partial^2 T^*}{\partial y^{*2}}\right) \tag{2-31}$$

where $x^* = x/L \quad y^* = y/L \quad t^* = t/(L/U) \quad T^* = (T-T_A)/(T_B-T_A) \quad \alpha = \dfrac{k}{\rho C_p}$.

2.5 Concentration equation

2.5.1 General species equations

Accoridng to Fick's law[4,5],

$$J = -D\cdot\frac{\partial C}{\partial x} \tag{2-32}$$

Where J represents diffusion flux, and D is the diffusion coefficient, C is the concentration in dimensions of mol/m^3.

When the fluid is a specific solution, the equation of concentration of the solution is (2-33)

$$\frac{\partial C}{\partial t} + u\frac{\partial C}{\partial x} + v\frac{\partial C}{\partial y} = D\left(\frac{\partial^2 C}{\partial x^2} + \frac{\partial^2 C}{\partial y^2}\right) \tag{2-33}$$

2.6 Convection-diffusion equation

Some the equations written above, (2-21) (2-29) (2-33) can be summarized in the convection-diffusion equation (2-34) or (2-35)

$$\frac{\partial \rho\phi}{\partial t} + \nabla(\rho \boldsymbol{u}\phi) = \nabla(\Gamma \nabla\phi) + S \tag{2-34}$$

$$\rho\frac{\partial \phi}{\partial t} + \rho u\frac{\partial \phi}{\partial x} + \rho v\frac{\partial \phi}{\partial y} = \frac{\lambda}{C_p}(\frac{\partial^2 \phi}{\partial x^2} + \frac{\partial^2 \phi}{\partial y^2}) + S \tag{2-35}$$

The accumulation of ϕ, plus the net convective flow, has to be the net diffusive flow plus the generation of ϕ per unit of volume. The diffusive term flows from greater to smaller value of ϕ.

Where $\rho\frac{\partial \phi}{\partial t}$ represents the temporary term, $\rho u\frac{\partial \phi}{\partial x} + \rho v\frac{\partial \phi}{\partial y}$ is convective term, $\frac{\lambda}{C_p}(\frac{\partial^2 \phi}{\partial x^2} + \frac{\partial^2 \phi}{\partial y^2})$ is diffusive term, and S is source term.

According to the convection diffusion equation, we can write an able with the appropriate parameters in order to rearrange the governing equations. As Table 2.1

Equation	ϕ	Γ	S
Continuity	1	0	0
Momentum in x direction	u	μ	$-\partial p_d/\partial x$
Momentum in y direction	v	μ	$-\partial p_d/\partial y+\rho g\beta(T-T_\infty)$
Energy(constant C_p)	T	λ/C_p	Φ/C_p
Concentration	C	D	0

Table 2.1 Parameters to replace in convection – diffusion equation in order to reproduce the governing equation.

Chapter 3: Discretization procedure

3.1 Mesh

3.1.1 Hyperbolic mesh

In a specific case, generally the flow is more drastic near boundary than other area. Hence instead of a uniform mesh a mesh with distance in term of hyperbolic function is applied to reduce simulation time with the same nodes. Equation (3-1) shows the function of distance in a hyperbolic mesh:

$$x(i) = \delta + \frac{\Delta\delta}{2}[1 + \tanh(2k_x \frac{\tilde{i}-1}{n} - k_x) / \tanh(k_x)] \quad (3\text{-}1)$$

Where $x(i)$ is the coordinate location at node i, δ is the distance from origin to the first node, k_x is concentration factor, what's more, for different types of concentration

a. Concentration symmetry: $n = N_r$, $\delta = x_r$, $\Delta\delta = L_r$, $\tilde{i} = \mathrm{i} - \mathrm{i_r} + 1$.

b. Concentration to right: $n = 2N_r$, $\delta = x_r$, $\Delta\delta = 2L_r$, $\tilde{i} = \mathrm{i} - \mathrm{i_r} + 1$

c. Concentration to left: $n = 2N_r$, $\delta = x_r - L_r$, $\Delta\delta = 2L_r$, $\tilde{i} = i + N_r - i_r + 1$.

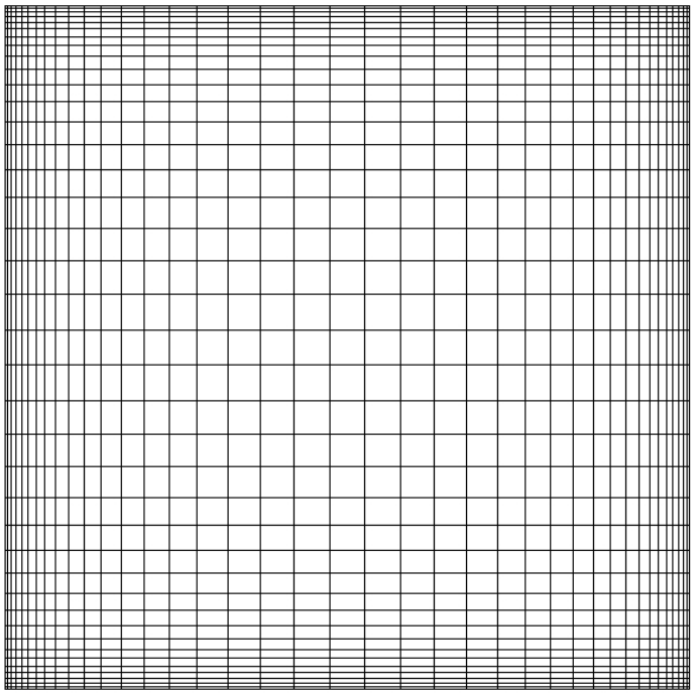

Fig 3.1.1 A typical hyperbolic mesh at 40*40 with concentration factor 2

3.2 Finite-Volume Method

The methodology of CFD generally consists basically of three parts: pre-processing, simulation and post-processing. In pre-processing, the geometry of the problem is defined, the volume occupied by the fluid is divided into a finite number of control volumes, the problem is modelled by its governing equations which are properly manipulated, usually aiming the obtaining of a set of linear equations, and finally the boundary and initial conditions are defined. The simulation process means solving the acquired linear equations iteratively and record the data necessary. In the end, post-processing step permits arrangement and visualization of the resulting solution.

There are varies of discretization method in CFD, some of the most used are as below:

Finite Element Method (FEM)

Finite Difference Method (FDM)

Finite Volume Method (FVM)

Spectral Method

The control equations in this paper will be solved by means of FVM. This method is commonly used in most general CFD codes due to its conservation properties, which guarantee the conservation principles in both unitary and global domain.

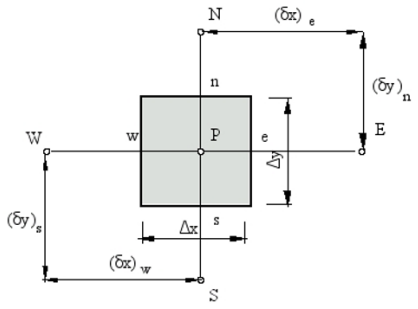

Fig 3.2.1 A control volume under FVM

Fig 3.2 shows a control volume under FVM, and in this control volume, for example the integrated foam of convection – diffusion equation is (3-1a), after FVM method the discretization equation is (3-1b)

$$\int_{\Omega}\rho\frac{\partial\phi}{\partial t}d\Omega+\int_{\Omega}\rho(\nabla\cdot\mathbf{v})d\Omega=\int_{\Omega}\Gamma\nabla^{2}\phi d\Omega+\int_{\Omega}Sd\Omega \qquad (3\text{-}1a)$$

In which from left to right, the terms are orderly transient term, convective term, diffusive term, and source term.

$$\frac{(\rho\phi)_P^{n+1}-(\rho\phi)_P^n}{\Delta t}\Delta x\Delta y+[(\rho u\phi)_e^{n+1}-(\rho u\phi)_w^{n+1}]\Delta y+[(\rho u\phi)_n^{n+1}-(\rho u\phi)_s^{n+1}]\Delta x$$
$$=[(\Gamma\frac{\partial\phi}{\partial x})_e^{n+1}-(\Gamma\frac{\partial\phi}{\partial x})_w^{n+1}]\Delta y+[(\Gamma\frac{\partial\phi}{\partial x})_n^{n+1}-(\Gamma\frac{\partial\phi}{\partial x})_s^{n+1}]\Delta x+S_P^{n+1}\Delta x\Delta y \quad (3\text{-}1b)$$

Where the following hypothesis are done:

1. In the integration process, the convective and diffusive flows have been considered constant through each face of the control volume.
2. (spatial deviation)^n=(spatial deviation)$^{n+1}$
   (spatial deviation)$_w$=(spatial deviation)$_e$
   (spatial deviation)$_s$=(spatial deviation)$_n$

3.2.1 Stagger mesh

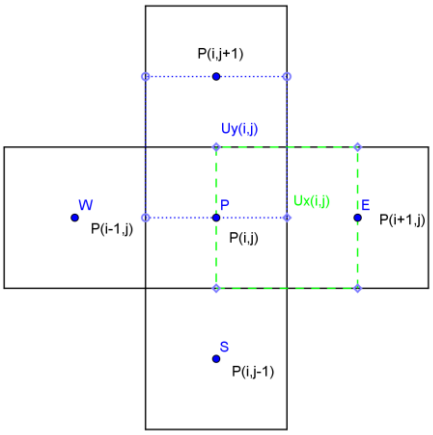

Fig 3.2.1 Stagger Mesh

In the momentum equation pressure and velocity are coupled, in order to avoid check board result, the velocity both in horizontal and vertical at the same domain are not taken as the same location of pressure. As showed in Fig 3.1.2, point P represents the pressure of the node, while the corresponding velocity is on the east and north face of the node.

3.3 Discretization of convective term

The discretization of the convective term from equation (2-13) is as (3-2)

Where divergence theorem and $\nabla \cdot \mathbf{u} = 0$ has been applied.

$$\int_{\Omega} \rho(\nabla \cdot \mathbf{v}) d\Omega = \int_{\Omega} \rho \nabla \cdot (v\phi) d\Omega = \int_{\Gamma} \rho(v\phi) \cdot n dS \tag{3-2}$$

$$\int (\rho\phi\mathbf{u}) \cdot \mathbf{n} \mathrm{d}s = (\rho\mathbf{u})_e \phi_e A_e - (\rho\mathbf{u})_w \phi_w A_w + (\rho\mathbf{u})_n \phi_n A_n - (\rho\mathbf{u})_s \phi_s A_s \tag{3-2}$$

Where $F_n = (\rho v)_n$ represents the mass flow rate on the corresponding cell face.

3.4 Discretization of diffusive term

According to divergence theorem, the integral diffusive term could be expressed as (3-3)

$$\int_{\Omega} \Gamma \nabla^2 \phi d\Omega = \int_{\Gamma} \Gamma \nabla \phi \cdot n \mathrm{d}S \tag{3-3}$$

$$\int (\Gamma \nabla \phi) \cdot n \mathrm{d}s = (\Gamma \nabla \phi)_e A_e - (\Gamma \nabla \phi)_w A_w + (\Gamma \nabla \phi)_n A_n - (\Gamma \nabla \phi)_s A_s \tag{3-3}$$

3.5 Discretization of transient term

The discretization of transient term could be obtained as equation (3-4)

$$\int \frac{\partial}{\partial t} (\rho\phi) \mathrm{d}V = \frac{(\rho\phi)^{n+1} - (\rho\phi)^n}{\Delta t} \Delta x \Delta y \tag{3-4}$$

3.6 Discretization of source term

The discretization of source term could be obtained as equation (3-5)

$$\int_{\Omega} S d\Omega = S_P \Delta x \Delta y \tag{3-5}$$

In which S_p means the source in the control volume, in momentum equation with Bousnesseq hypothesis this term will conclude Bouyance term besides the pressure term.

3.7 Numerical scheme

3.7.1 Introduction

In the process of discretization, linear equations will replace differential equation on a certain mesh where the values of different variables at points and interfaces are determined by numerical schemes.

3.7.2 Different schemes

a. Low order numerical schemes

In equation (3-1), convective and diffusive terms are evaluated at the cell faces, whereas dependent variable ϕ is known at the cell center. The evaluation of the variable at the cell face is carried out by schemes.

Conductive flux is calculated as an arithmetic mean:

$$(\frac{\partial \phi}{\partial x})_e = \frac{\phi_E - \phi_P}{\delta x_e} \; or \; (\frac{\partial \phi}{\partial x})_e = \frac{\phi_E - \phi_P}{\delta x_e} \tag{3-2}$$

The order of a numerical scheme is the number of neighbour nodes that are used to evaluate dependent variables at the cell face.

Central difference Scheme (CDS): It is a second order scheme, variable at the cell face is calculated as an arithmetic mean. That is:

$$\phi_e = \frac{\phi_E + \phi_P}{2} \tag{3-3}$$

Upwind Difference Scheme (UDS): It is a first order scheme and the value of ϕ at the cell face is equal to the value of ϕ at the grid point on the upwind side of the face. That is:

$$\begin{aligned} \phi_e &= \phi_P \qquad \text{if} \quad F_e > 0 \\ \phi_e &= \phi_E \qquad \text{if} \quad F_e < 0 \end{aligned} \tag{3-4}$$

Hybrid Difference Scheme (HDS): Uses CDS for low velocities and UDS for high velocities.

Exponential Difference Scheme (EDS): It is a second order scheme and the evaluation of the dependent variable at the cell face comes from the exact solution of the convection-diffusion equation in one-dimensional, null source term and steady problem.

Powerlaw Difference Scheme (PLDS): It is a second order scheme and variable at the cell face is calculated with an approximation of the EDS by a polynomial of fifth degree.

b. High order numerical scheme

If dependent variable is normalized as:

$$\bar{\phi}_f = \frac{\phi_f - \phi_U}{\phi_D - \phi_U} \tag{3-5}$$

Where ϕ_D is value of ϕ at the nearest grid point on the downstream side of the face, ϕ_U is value of ϕ at the grid point above ϕ_C, ϕ_C is value of ϕ at the nearest grid point on the upstream side of the face, as showed in Fig 3.3.1[6].

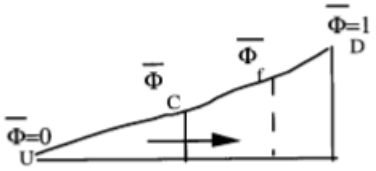

Fig 3.7.1 Sketch of normalized variables profile

If cell face is not at the middle between two nodal points, it is necessary to introduce geometric variables. Thus, distances are normalized in a similar form:

$$\bar{x}_f = \frac{x_f - x_U}{x_D - x_U} \tag{3-6}$$

The problem only depends on three variables (3-7):

$$\phi_f = \mathrm{f}(\phi_U, \phi_C, \phi_D, x_U, x_C, x_f, x_D) \rightarrow \bar{\phi} = \mathrm{f}(\bar{\phi}_C, \bar{x}_C, \bar{x}_f) \tag{3-7}$$

Quick scheme is upstream quadratic interpolation scheme which uses three point weighted quadratic interpolation to obtain cell face value; the face value ϕ_f is obtained from quadratic function passing through two bounding nodes and one node upstream. The expression for determining using normalized variable is shown in (3-5) (3-6), hence, the final expression:

$$\phi_f = \bar{x}_f + \frac{\bar{x}_f(\bar{x}_f - 1)}{\bar{x}_C(\bar{x}_C - 1)}(\bar{\phi}_C - \bar{x}_C) \tag{3-8}$$

The quick scheme is third order accuracy, which retain transportability. But drawback of this scheme is instability problem which may cause minor undershoot or overshoot, so the resulting solution is not bounded[7].

To solve instability problem in the quick scheme, smart scheme was introduced. It is second to fourth order accuracy. It is composed by quick straight line, a portion of the

downwind line close to (Øf = 1), and a straight line with slope 3 connecting to (Øf = 0) [8].

$$\bar{\phi}_f = \begin{cases} \dfrac{\bar{x}_f(1-3\bar{x}_C+2\bar{x}_f)}{\bar{x}_C(1-\bar{x}_C)}\bar{\phi}_C, & 0 < \bar{\phi}_C \le \dfrac{\bar{x}_C}{3} \\ \bar{x}_f + \dfrac{\bar{x}_f(\bar{x}_f-1)}{\bar{x}_C(\bar{x}_C-1)}(\bar{\phi}_C-\bar{x}_C), & \dfrac{\bar{x}_C}{3} \le \bar{\phi}_C \le \dfrac{\bar{x}_C(1-\bar{x}_C+\bar{x}_f)}{\bar{x}_f} \\ 1, & \dfrac{\bar{x}_C(1-\bar{x}_C+\bar{x}_f)}{\bar{x}_f} \le \bar{\phi}_C \le 1 \\ \phi_C, & \text{otherwise} \end{cases} \qquad (3\text{-}9)$$

Chapter 4: Algorithm for pressure velocity coupling problem

4.1 Introduction of FSM

The fractional step methods has become a very popular technique for solving the incompressible Navier-Stokes equation[9,10,11]. This method is also known as the projection method for solving the Navier-Stokes equations because equations are interpreted as projection into a divergence-free velocity space. Predictor velocity is firstly obtained by convective-diffusive equation in which there is no contribution from pressure, so it does not satisfy the incompressibility constraint in the next time step. Then the Poisson equation is solved to get the pressure, which is used to correct the predictor velocity to satisfy the incompressibility constraint.

4.2 Algorithm for FSM

From equation (2-5)(2-6), to make the expression more compact, the equation could be written as below:

$$\frac{\partial u}{\partial t} = R(u) - \nabla p \tag{4-1}$$

Where $R(u) = -(u \cdot \nabla) + \frac{1}{Re}\Delta u$.

For the temporal discretization, a central difference scheme is used for the time derivative term,

$$\frac{\partial u}{\partial t}^{n+1/2} \approx \frac{u^{n+1} - u^n}{\Delta t} + \mathrm{O}(\Delta t^2) \tag{4-2}$$

a fully explicit second-order Adams-Bashforth scheme for $R(u)$

$$R^{n+1/2}(u) \approx \frac{3}{2} R(u^n) - \frac{1}{2} R(u^{n-1}) + \mathrm{O}(\Delta t^2, \Delta x^m) \tag{4-3}$$

and a first-order backward Euler scheme for the pressure-gradient term. Incompressibility constraint is treated implicitly. Thus, we obtain the semi-discretized Navier-Stokes equations. To solve the velocity-pressure coupling we use a classical fractional step projection method [12,13]

$$\frac{u^{n+1}-u^n}{\Delta t}=\frac{3}{2}R(u^n)-\frac{1}{2}R(u^{n-1})-\nabla p^{n+1} \tag{4-4}$$

$$\nabla\cdot u^{n+1}=0 \tag{4-5}$$

The Helmholtz-Hodge decomposition theorem is applied to the incompressible Navier-Stokes equations as equation (4-6)

$$\Pi(\frac{\partial u}{\partial t}+\nabla p)=\Pi(-u(u\cdot\nabla)+\frac{1}{Re}\Delta u) \tag{4-6}$$

Where $\Pi(\frac{\partial u}{\partial t})=\frac{\partial u}{\partial t}$, $\Pi(\nabla p)=0$, Navier-Stokes equations can be split in two parts: a divergence-free vector and a gradient of a scalar field, as showed in Fig 4.1, resulting in (4-7) (4-8).

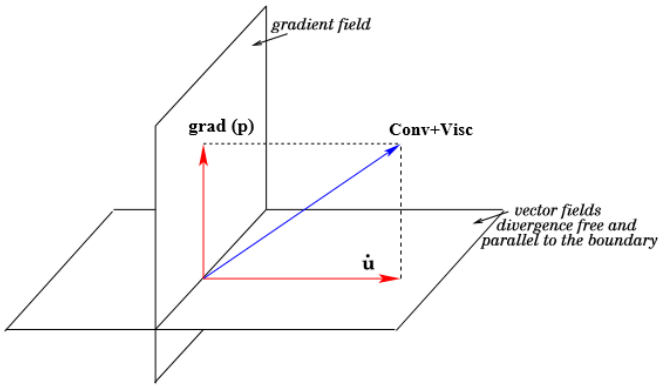

Fig 4.2.1 Convective + Viscous term vector field unique decomposition

$$\frac{\partial u}{\partial t}=\Pi(-u(u\cdot\nabla)+\frac{1}{Re}\Delta u) \tag{4-7}$$

$$\nabla p=-(u\cdot\nabla)u+\frac{1}{Re}\Delta u-\Pi(-u(u\cdot\nabla)+\frac{1}{Re}\Delta u) \tag{4-8}$$

Hence, applying the divergence operator to (4-8) leads to a Poisson equation for pressure

$$\Delta p=\nabla(-u(u\cdot\nabla)+\frac{1}{Re}\Delta u) \tag{4-9}$$

if we assume predictor velocity $u^p=u^{n+1}+\nabla\tilde{p}$ and pseudo pressure $\tilde{p}=\Delta t p^{n+1}$, (4-4)(4-5) will lead to (4-10)(4-11)

$$u^p = u^n + \Delta t(\frac{3}{2}R(u^n) - \frac{1}{2}R(u^{n-1})) \quad (4\text{-}10)$$

$$\nabla \cdot u^p = \nabla \cdot u^{n+1} + \nabla \cdot (\nabla \tilde{p}) \rightarrow \Delta p = \nabla \cdot u^p \quad (4\text{-}11)$$

Once the solution of pressure is obtained, new velocity field could be resulted from the correction

$$u^{n+1} = u^p - \nabla \tilde{p} \quad (4\text{-}12)$$

Therefore, the calculate procedure of each time step is

a. Evaluate $R(u^n)$.
b. Evaluate u^p form (4-10)
c. Solve the Poisson equation (4-11)
d. Obtain new velocity field from (4-12)

4.3 Determination of time step

Due to stability reason, explicit temporal schemes may introduce severe restrictions on the time step, while implicit discretization would improve the overall stability. The final performance of time-integration method would be case dependent: for instance, the use of implicit methods in DNS/LES of turbulent flows the computational costs are rather high compared to those of explicit methods. This is because of the underlying restrictions to time step that are required to fully resolve all temporal scales in the Navier-Stokes equations [14, 15, 16]. On the other hand, implicit methods are very convenient for pseudo-transient simulations of laminar steady flows [17]. Here, we have only considered explicit method in the view of formulation simplicity.

Therefore, in our case, the time-step, Δt, must be bounded by the CFL condition [18] given by where the bounding values C_{conv} are C_{visc} must be smaller than unity. In our case, we will follow the recommendations given by [19] using values $C_{conv} = 0.35$ and $C_{visc} = 0.2$, respectively.

Chapter 5: Reference case result

5.1 Driven cavity

5.1.1 Problem description

Driven cavity problem is a classic simulation case in fluid dynamic, which is showed at Fig 5.1.1, a square cavity placed in a x-y plane with the lid move at x-direction speed *U*, in the dimensionless equation the velocity will be 1.0, the other walls are non-slip boundary.

The boundary condition of the walls is Neumann boundary, which means at the wall $\frac{\partial p}{\partial n} = 0$, the pressure of the walls must be set with a reasonable value to avoid unexcepted problem in the solver, hence the pressure of the wall is set the same as the inner fluid.

The problem will be solved at different *Re* number, 100,1000,5000, and different numerical schemes like up-wind, central difference, Quick, smart grid. The result will be compared with the benchmark solution.

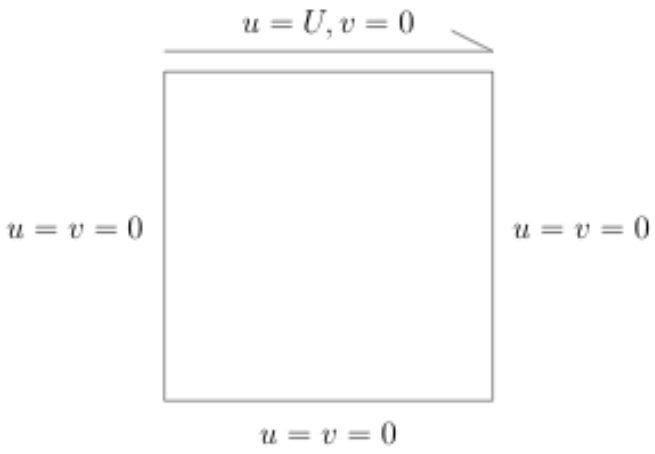

Fig 5.1.1 Geographic sketch of Lid Driven Cavity

5.1.2 Result and discussion

Fig 5.1.2 and Fig 5.1.3 reveal the velocity distribution on mid x-plane and y-plane, in which the result contains four numerical schemes at the same uniform mesh 50*50. In the figure we could see that smart grid performs better than others, and the rest of the

simulation will employ smart grid to get more accurate result especially for the high *Re* numbers cases.

Fig 5.1.4 – Fig 5.1.9 demonstrate the velocity of *x*,*y* coordinate along the vertical and horizontal line through the cavity. The result from the code match perfectly to the benchmark result [20].

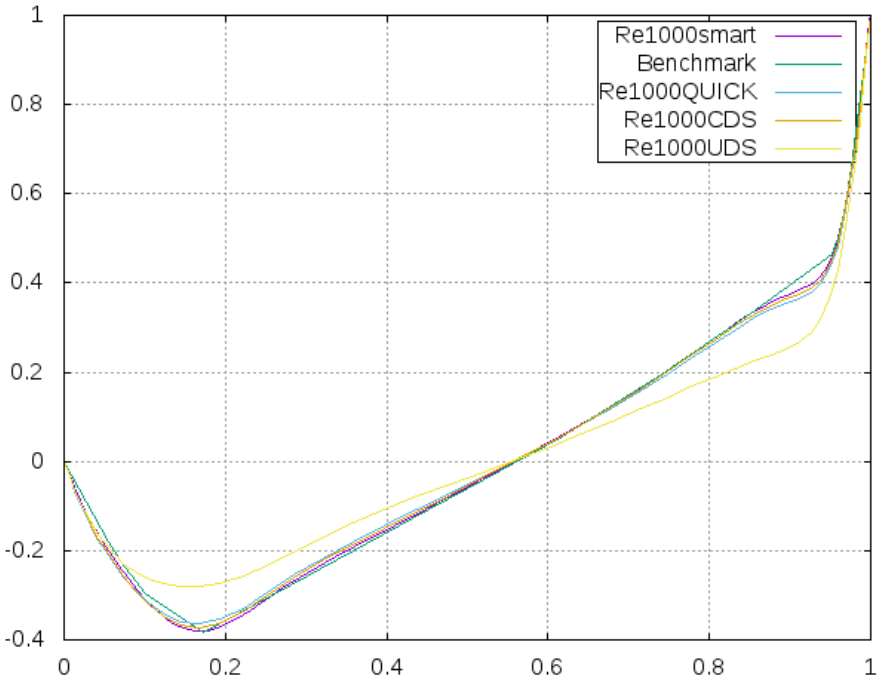

Fig 5.1.2 *Ux* on *y* mid plane at *Re* 1000 with different schemes

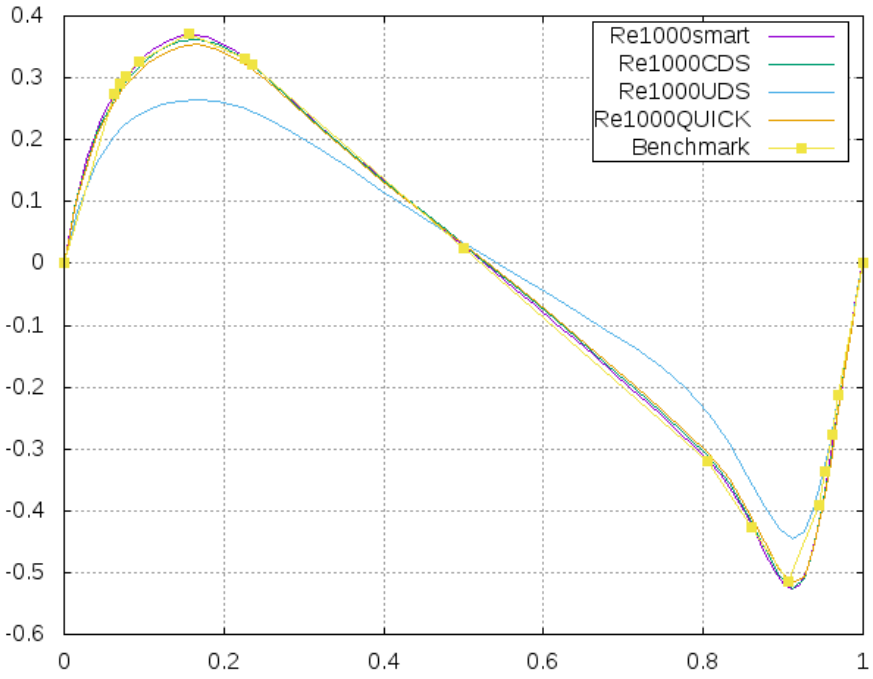

Fig 5.1.3 *Uy* on *x* mid plane at *Re* 1000 with different schemes

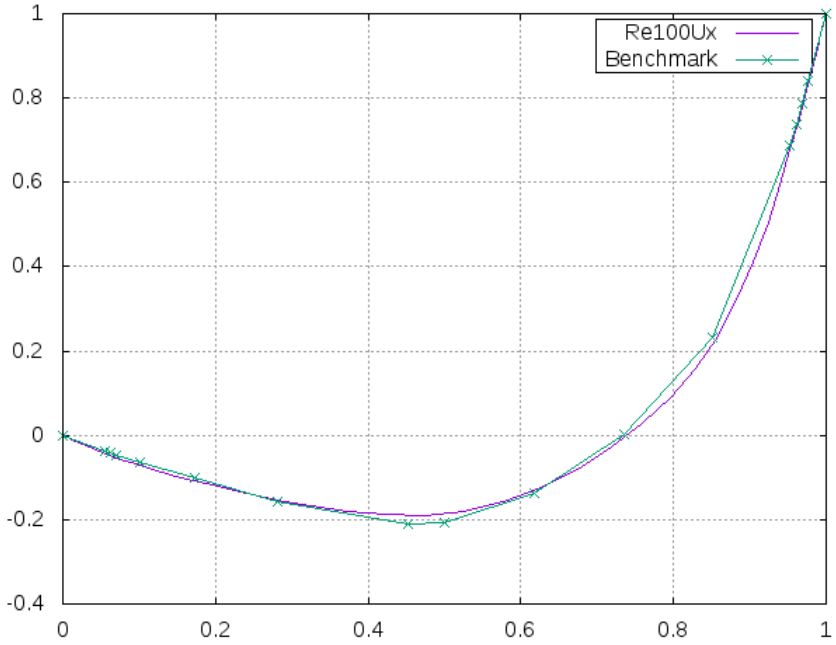

Fig 5.1.4 *Ux* on *y* mid plane compared with Benchmark solution at *Re* 100

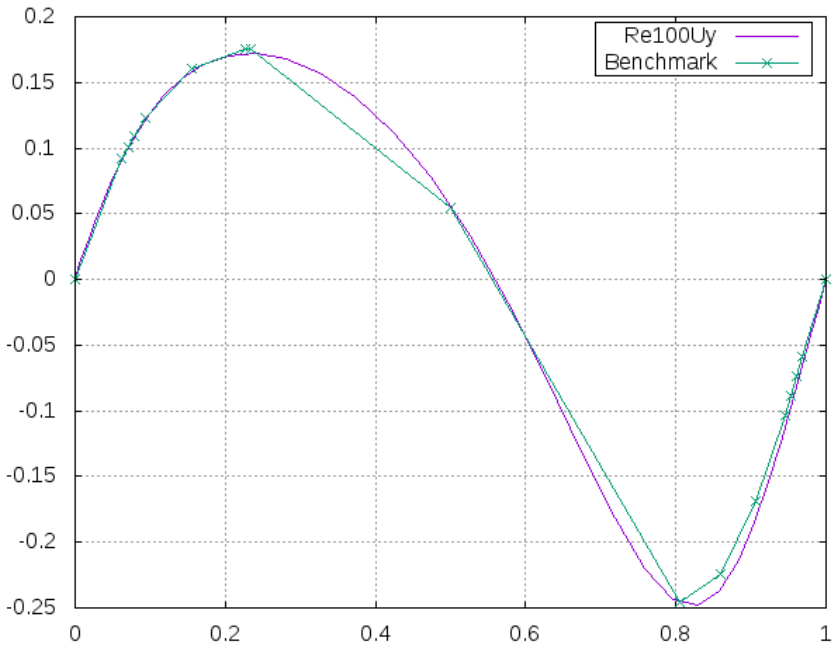

Fig 5.1.5 *Uy* on *x* mid plane compared with Benchmark solution at *Re* 100

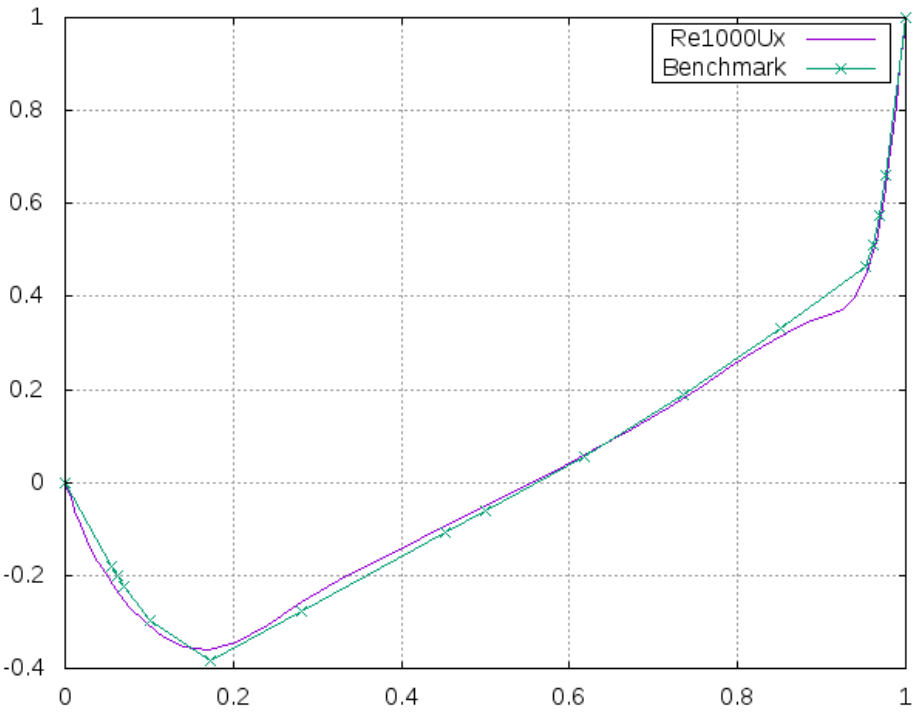

Fig 5.1.6 *Ux* on *y* mid plane compared with Benchmark solution at *Re* 1000

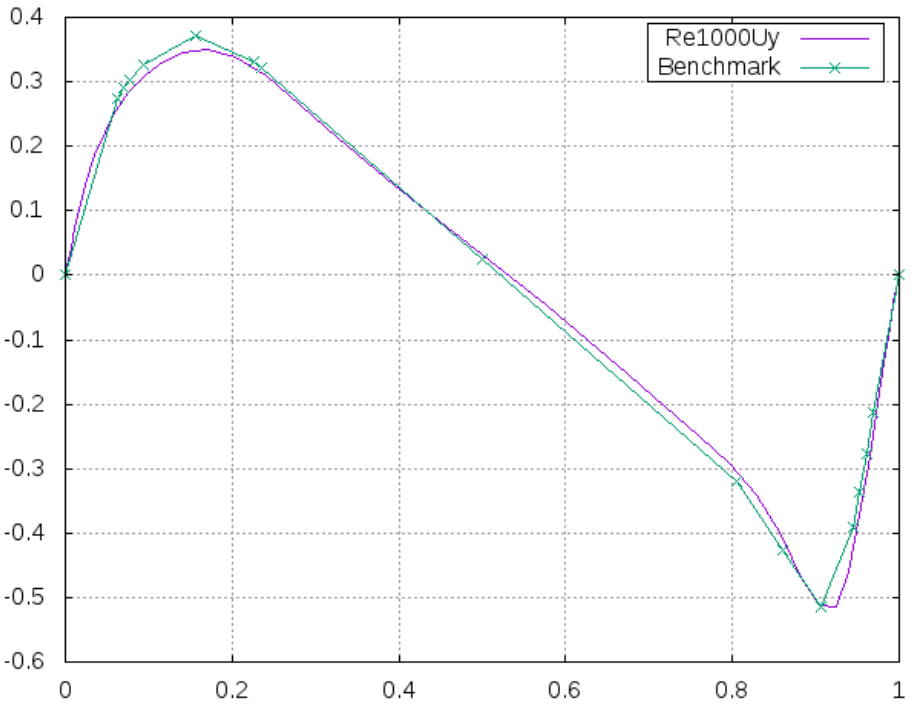

Fig 5.1.7 *Uy* on *x* mid plane compared with Benchmark solution at *Re* 1000

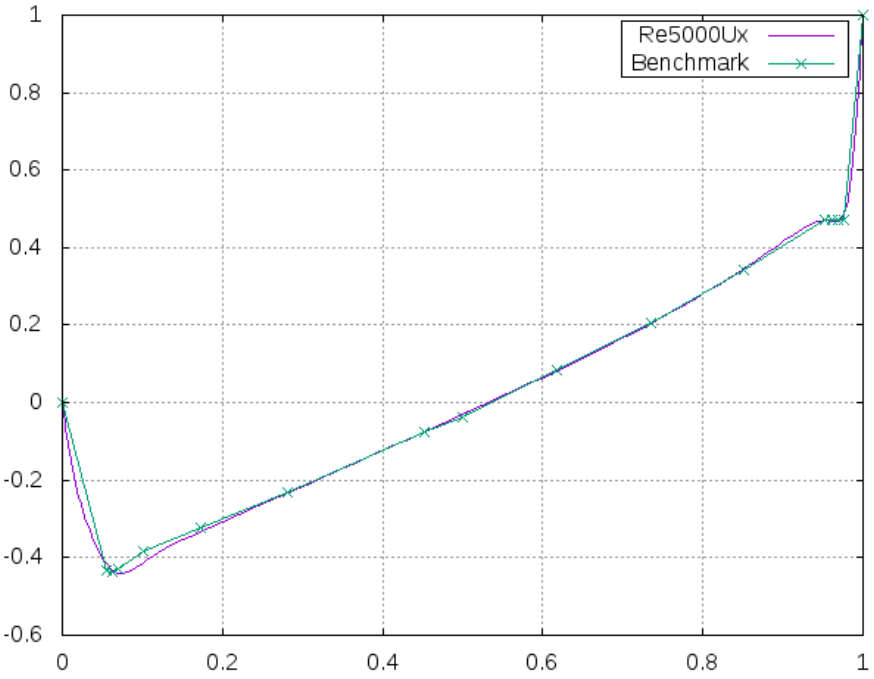

Fig 5.1.8 *Ux* on *y* mid plane compared with Benchmark solution at *Re* 5000

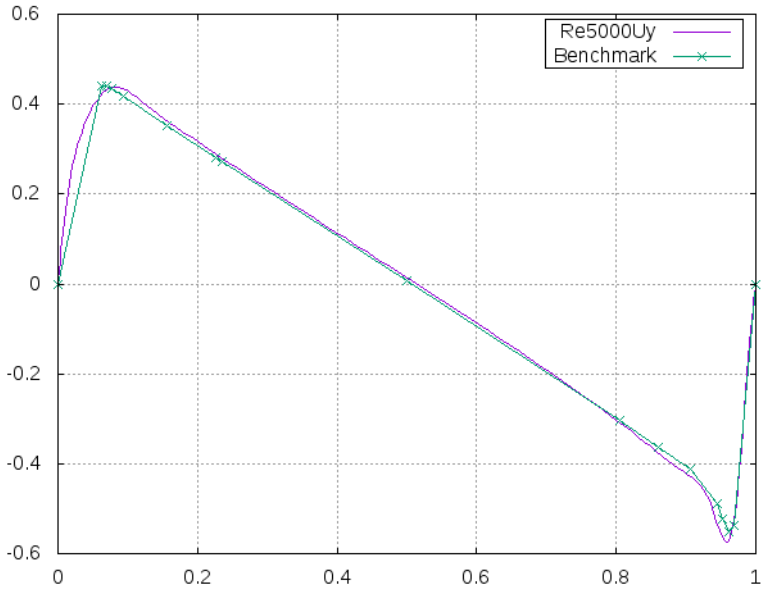

Fig 5.1.9 *Uy* on *x* mid plane compared with Benchmark solution at *Re* 5000

Fig 5.1.10 – Fig 5.1.16 show the contours of velocities profile and streamlines at different *Re* numbers.

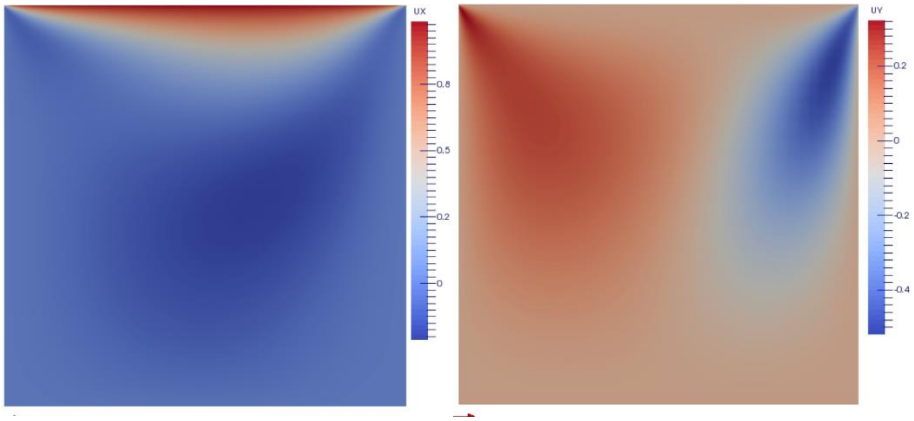

(a) *Ux* (b) *Uy*

Fig 5.1.10 Contours plot of *Ux* and *Uy* in the Cavity at *Re* 100

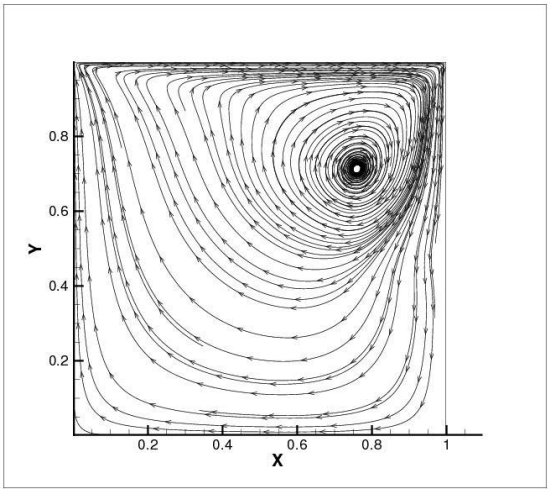

Fig 5.1.11 Streamline at *Re* = 100

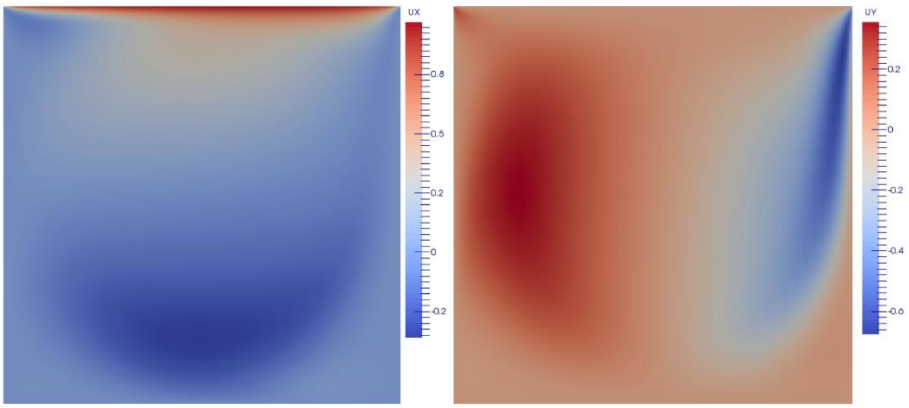

(a) *Ux* (b) *Uy*

Fig 5.1.12 Contours plot of *Ux* and *Uy* in the Cavity at *Re* = 1000

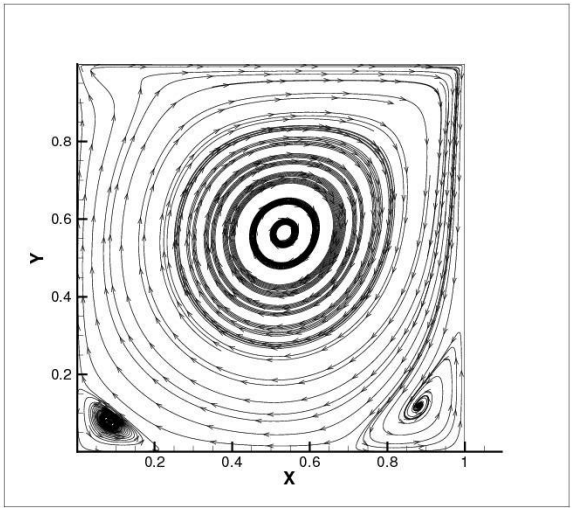

Fig 5.1.13 Streamline at *Re* = 1000

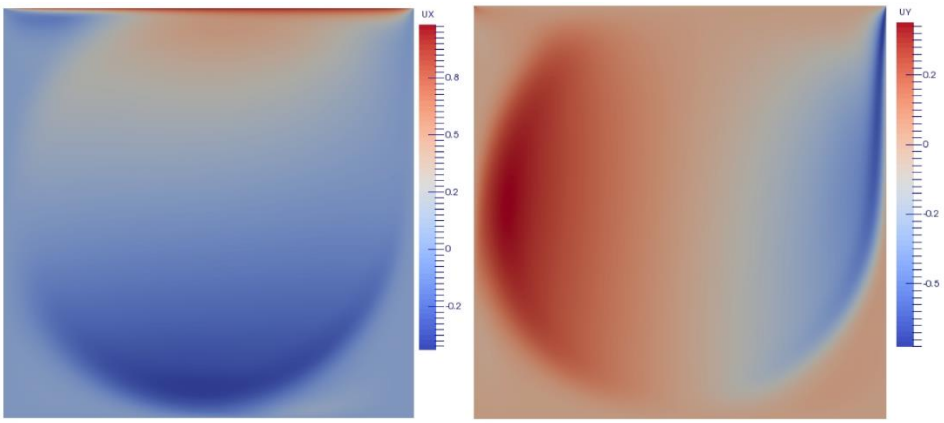

(a) *Ux* (b) *Uy*

Fig 5.1.14 Contours plot of *Ux* and *Uy* in the Cavity at *Re* = 5000

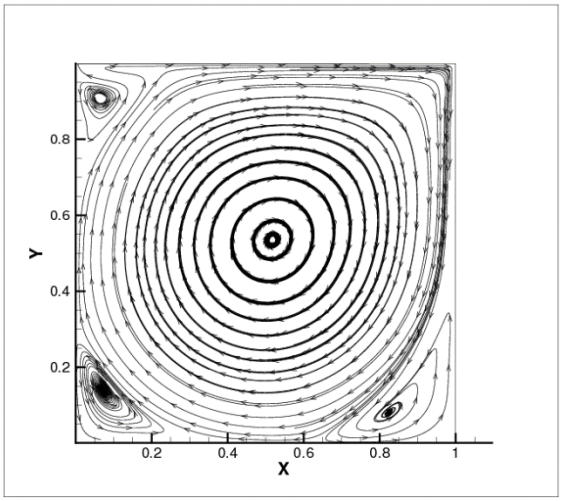

Fig 5.1.15 Streamline at *Re* = 5000

5.2 Differentially heated square Cavity

5.2.1 Problem description

The geometry of the problem is showed as Fig below, an upright square cavity of which the left wall is isothermal at T_h while the right wall at T_c, both top and bottom sides are insulation. Bossinseq approximation for natural convection is considered in y -direction and the Prandtl number is 0.71. Both momentum and energy equation will be solved in this case in a dimensionless equation at different Ra number, 10^3, 10^4, 10^5 and 10^6.

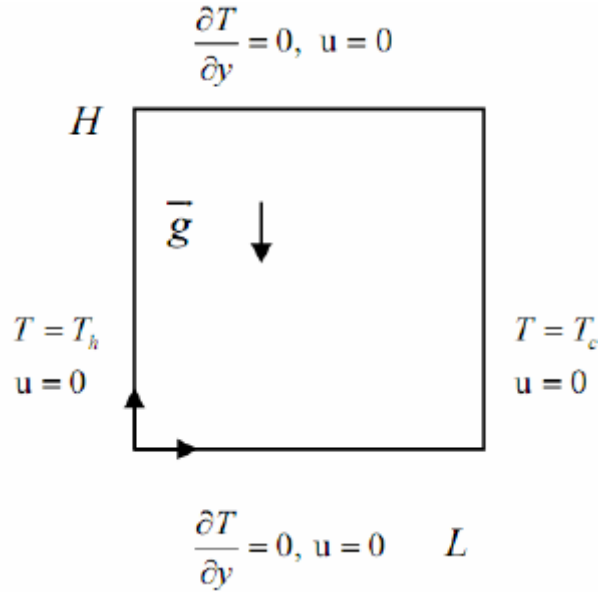

Fig 5.2.1 Geographic sketch of Differentially Heat Cavity

5.2.2 Result

Table 5.1 shows the result at *Ra* 1000, and compared with Benchmark solution [21,22]

Fig 5.2.2, 5.2.3 show the distribution of velocities, temperature and streamlines:

Ra	1000		
	Bench	Result	Error
$\|\psi\|$mid	1.174	1.175	0.09%
u_{max}	3.649	3.65	0.03%
y	0.813	0.82	0.85%
v_{max}	3.697	3.71	0.35%
x	0.178	0.18	1.11%
$\overline{Nu}$	1.118	1.118	0.00%
$Nu_{1/2}$	1.118	1.118	0.00%
Nu_0	1.117	1.118	0.09%
Nu_{max}	1.505	1.51	0.33%
y	0.902	0.9	0.22%
Nu_{min}	0.692	0.693	0.14%
y	1	0.99	1.01%

Table 5.1 Results compared to benchmark solution at *Ra* 1000

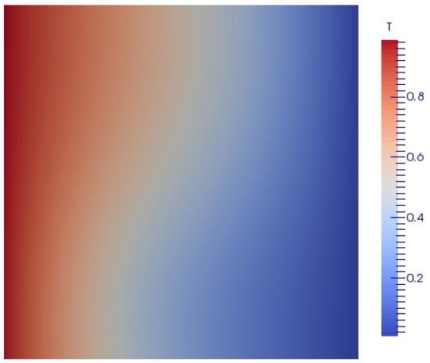

Fig 5.2.2 Contours of Temperature at *Ra* = 1000

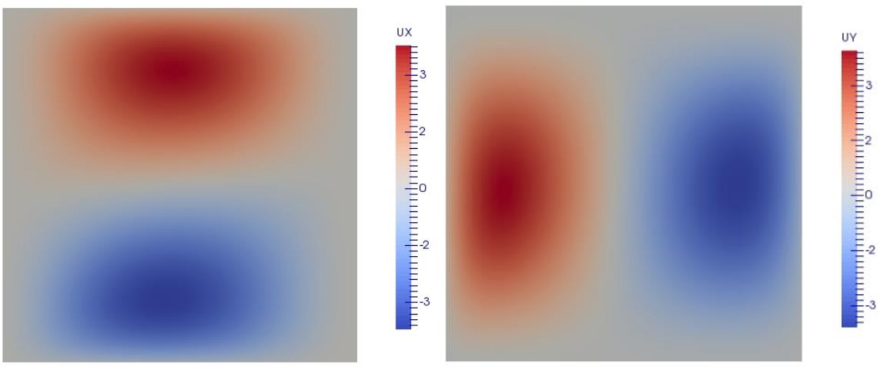

(a) *Ux* (b) *Uy*

Fig 5.2.3 Contours of Velocities at *Ra* = 1000

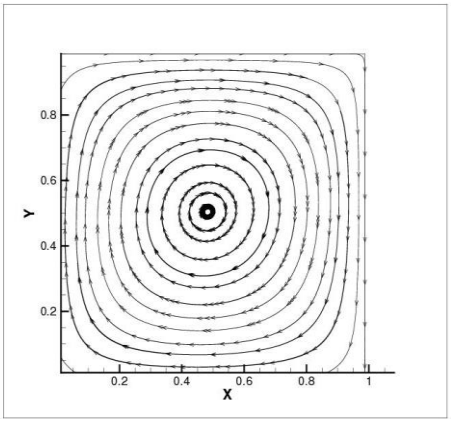

Fig 5.2.4 Streamline at *Ra* = 1000

Ra	10000		
	Bench	Result	Error
$\lvert\psi\rvert$mid	5.071	5.076	0.10%
u_{max}	16.178	16.191	0.08%
y	0.823	0.825	0.24%
v_{max}	19.617	19.59	0.14%
x	0.119	0.12	0.83%
$\overline{Nu}$	2.243	2.248	0.22%
$Nu_{1/2}$	2.243	2.248	0.22%
Nu_0	2.238	2.242	0.18%
Nu_{max}	3.528	3.541	0.37%
y	0.143	0.145	1.38%
Nu_{min}	0.586	0.579	1.21%
y	1	0.995	0.50%

Table 5.2 Results compared to benchmark solution at *Ra* 10000

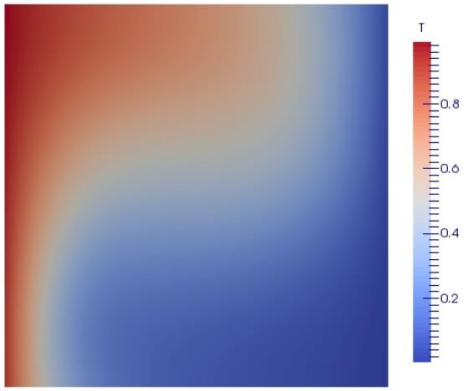

Fig 5.2.5 Contours of Temperature at *Ra* = 10000

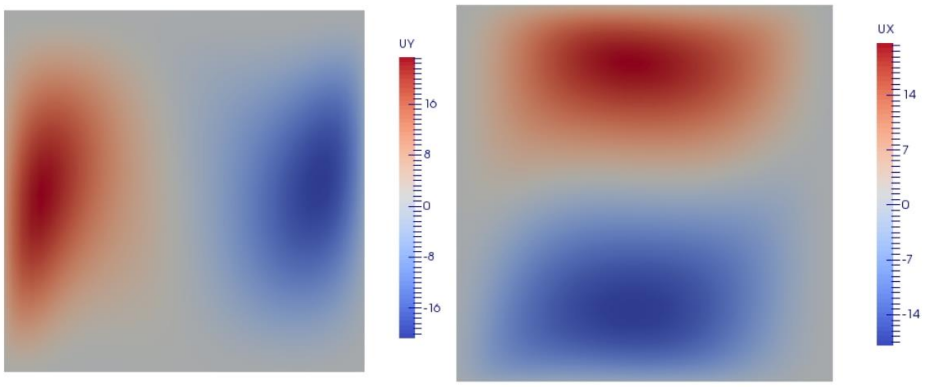

(a) *Ux* (b) *Uy*

Fig 5.2.6 Contours of velocities at *Ra* = 10000

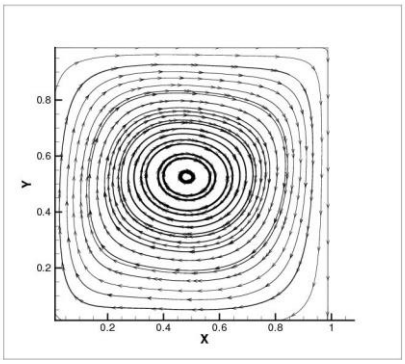

Fig 5.2.7 Contours of Temperature at *Ra* = 10000

Ra	100000		
	Bench	Result	Error
$\|\psi\|$mid	9.111	9.21	1.07%
$\|\psi\|$max	9.612	9.595	0.18%
x	0.285	0.285	0.00%
y	0.601	0.595	1.01%
u_{max}	34.73	34.786	0.16%
y	0.855	0.865	1.16%
v_{max}	68.59	71.53	4.11%
x	0.066	0.069	4.35%
$\overline{Nu}$	4.519	4.61	1.97%
$Nu_{1/2}$	4.519	4.61	1.97%
Nu_0	4.509	4.556	1.03%
Nu_{max}	7.717	7.812	1.22%
y	0.081	0.08	1.25%
Nu_{min}	0.729	0.701	3.99%
y	1	0.995	0.50%

Table 5.3 Results compared to benchmark solution at *Ra* 100000

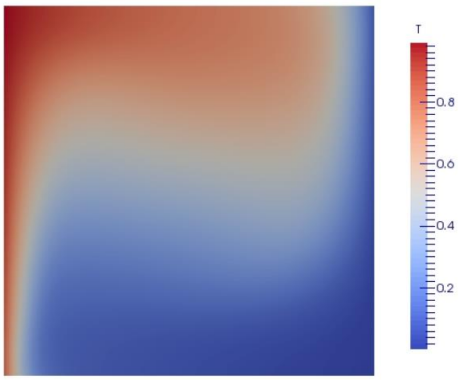

Fig 5.2.8 Contours of Temperature at *Ra* = 100000

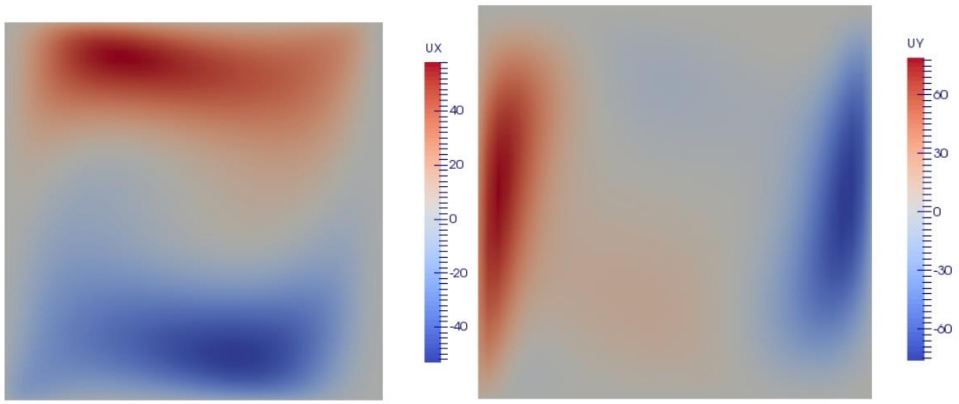

Fig 5.2.9 Contours of velocities at *Ra* = 100000

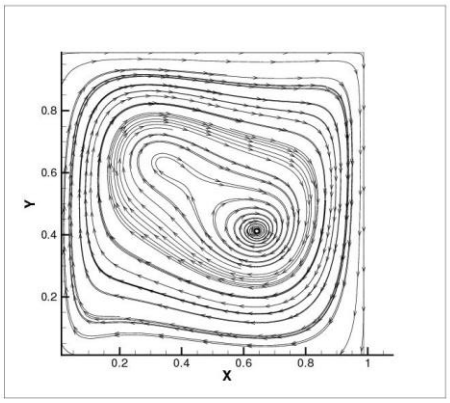

Fig 5.2.10 Contours of Temperature at *Ra* = 100000

5.3 Square cylinder problem

The flow past bluff bodies, square blockage in this case, is investigated in this problem. This part will focus on the performance of the flow after sweeping past a specific blockage under different *Re* number.

5.3.1 Problem description

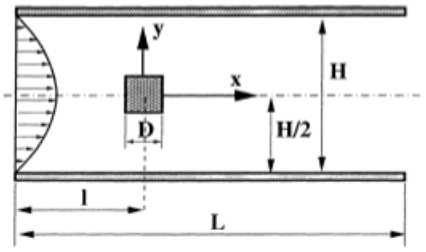

Fig 5.3.1 Sketch of square cylinder proble

As showed in Fig, the square blockage ratio was fixed at *B*=1/8. In order to reduce the influence of inflow and outflow, the length of the channel is set as L/D = 50. Inflow length *l* is set as *L*/*l* = 4, in [23], the influence of inflow length is almost negligible, and the blockage is placed at *H*/2 height.

5.3.2 Solution procedure

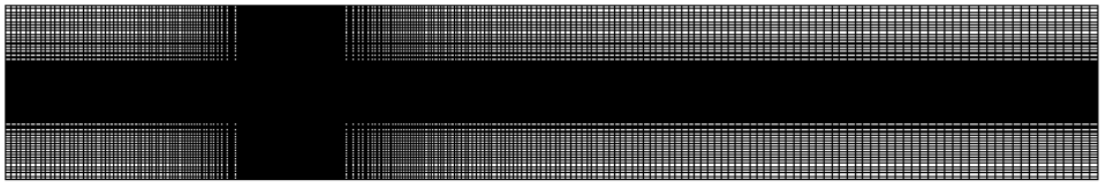

Fig 5.3.2 Hyperbolic mesh for Square cylinder problem

The inlet flow is considered as a fully developed laminar flow, thus a parabolic velocity profile with a maximum velocity u_{max} is set. A convection outflow condition is set to the outlet:

$$\frac{\partial u_i}{\partial t} + u_{conv} \frac{\partial u_i}{\partial x} = 0 \tag{5-1}$$

Both top and bottom wall are non-slip wall.

This problem will be solved by the same algorithm as Driven Cavity, meanwhile a sparse LU solver is employed here to reduce the computational time when the mesh is very fine.

5.3.3 Post -processing parameters

a. Recirculation lenth

The length of the closed near-wake is measured here for the blockage, eliminating the effect of blockage by extrapolation the blockage ration $B \to \infty$. Then the empirical relationship is linear [24]

$$Lr / D = 0.05\,\mathrm{Re} \qquad 4.4 < Re < 40 \tag{5-2}$$

b. Drag and lift coefficient

In the computational external flow analysis, drag and lift coefficient are very important characteristics and defined as below:

$$C_d = \frac{F_d}{\frac{1}{2}\rho u_\infty^2 D} \tag{5-3}$$

$$C_l = \frac{F_l}{\frac{1}{2}\rho u_\infty^2 D} \tag{5-4}$$

The drag force is a force impact on the blockage along the inlet flow direction while the lift force is on a perpendicular direction associated with the inflow. These two force could be integrated on the impact volume and leads to two coefficients[25].

$$F_x = \int_{S_b} p n_x \mathrm{d}s - \mu \int_{S_b} [2\frac{\partial u}{\partial x}, (\frac{\partial u}{\partial y} + \frac{\partial v}{\partial x})] \cdot \vec{n}\,\mathrm{d}s \tag{5-5}$$

$$F_y = \int_{S_b} p n_y \mathrm{d}s - \mu \int_{S_b} [(\frac{\partial u}{\partial y} + \frac{\partial v}{\partial x}), 2\frac{\partial v}{\partial y}] \cdot \vec{n}\,\mathrm{d}s \tag{5-6}$$

d. Strouhal number

Strouhal number is a dimensionless number measuring frequency of the vortex shedding f and the maximum velocity $u_{\max}$ at the flow plane. the vortex shedding frequency f was determined by a spectral analysis (fast Fourier transformation, FFT) of time series of the lift coefficient Cl.

$$St = \frac{fD}{u_{\max}} \tag{5-7}$$

5.3.4 Result

Fig 5.3.3 shows the recirculation length at *Re* number form 1to 60, and the three lines represent different value at mesh 300*150 and 200*100 by this paper comparing with the result of Breuer[23]. Hence, the data match well with the resolution and the correlation is obtained:

$$L_r / D = -0.099856 + 0.05592Re \qquad 5 \le Re \le 60 \tag{5-8}$$

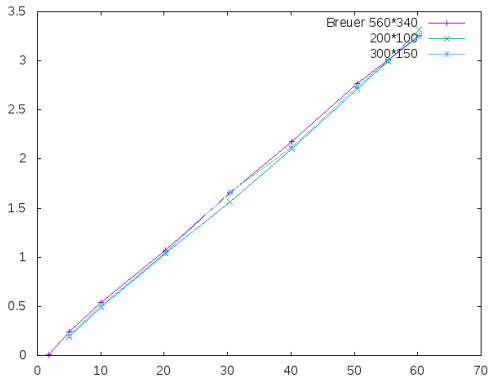

Fig 5.3.3 Recirculation length at Different *Re*

Fig 5.3.4 shows the drag coefficient of this paper at different meshes and compared with the result of [23]. From which we could easily see the trend of these two results matched well and the drag coefficient decrease when *Re* increase owing to the diminish in both pressure and viscous force.

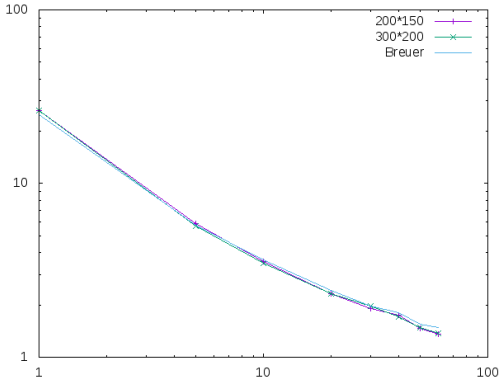

Fig 5.3.4 Drag coefficient at different *Re*

When the *Re* number succeed 60 the fluid is no longer steady, a sinusoidal oscillation commenced in the near wake shear layer, later forming the von Kármán vortex street. Fig 5.3.9 – Fig 5.3.11 show the evolution of pressure, velocities along *Re* number

ascending. As time passes, in the unsteady flow near wake the vortex will form and leave which leads to the periodic variation of both drag and lift force, and the aggregation of lift force in one period will be zero. Fig 5.3.5 shows the evolution of both in *Re* at 100 200, and it is clearly demonstrated that this oscillation grows faster in higher *Re* number.

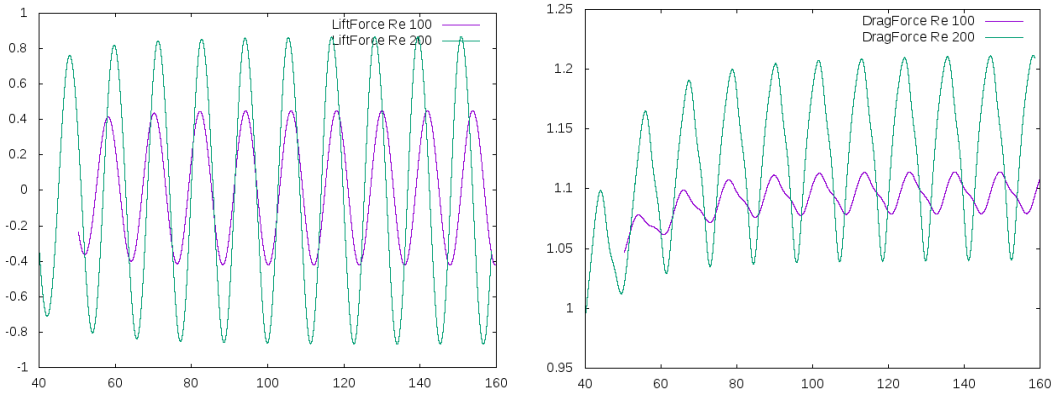

(a) Drag Coefficient (b) Lift Coefficient

Fig 5.3.5 Drag and lift coefficient evolution along time at *Re* 100,200

Fig 5.3.6 shows the *St* number with *Re* number, different meshes are used here to compare with the result in the previous work. *St* number hikes in *Re* range 60-140, and will acquire a peak value with Re around 140-160, after that, the *St* will decrease.

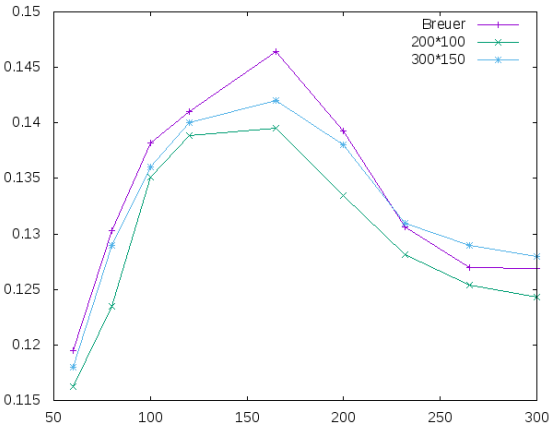

Fig 5.3.6 St number at different *Re* number

As showed in Fig 5.3.5, when the unsteady flow reaches a certain periodic frequency, in order to analyzes the force coefficient, the maximum difference in one period of force evolution is acquired and plotted with *Re* as Fig 5.3.7. Form which we could acknowledge that the maximum elevated drastically with the increment of *Re*, like an exponential function.

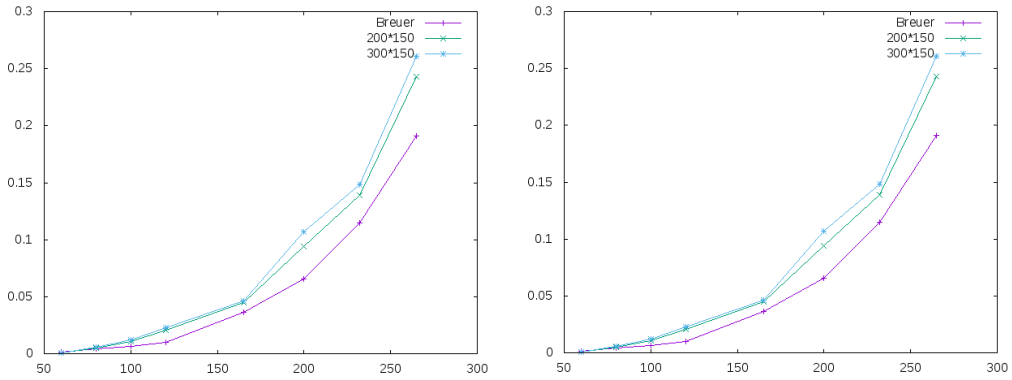

(a) $\max(C_d) - \max(C_d)$ (b) $\max(C_l) - \max(C_l)$

Fig 5.3.7 Variation of force coefficient at different *Re*

In Fig 5.3.4 and Fig 5.3.8, the drag coefficient decreased in the *Re* range 1-150, and around 150-160 C_d reached a minimum, after that it proceeded increasing. But in this work the C_d at biggest *Re* 300 is still far smaller than *Re* 1.

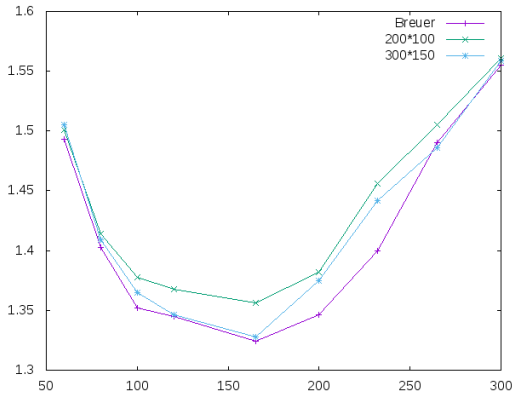

Fig 5.3.8 Drag coefficient at different *Re*

Fig 5.3.9 – Fig 5.3.11 show the streamlines around the square blockage and compared with the previous work at *Re* 1,60,200. At low *Re* number like 1, the creeping steady flow past the cylinder without separation [24] at *Re* 5, in a circular cylinder the separation of the flow pattern is discovered, which means in a sharp-edge obstacle lower *Re* could be detected. When *Re* increases, vortex forms in the back of the blockage like showed in Fig 5.3.10 but will not leave. In [26] a critical Re_{crit} around 54 was proposed, and vortex shedding could be seen when $Re > Re_{crit}$ as Fig 5.3.11. As the further ascending of *Re*, the free shear layers begin to roll up in the backward of the obstacle at Re = 100 like in the Fig 5.3.13 (d), which is known as von Kármán vortex street.

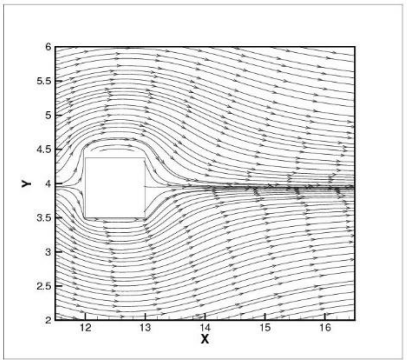

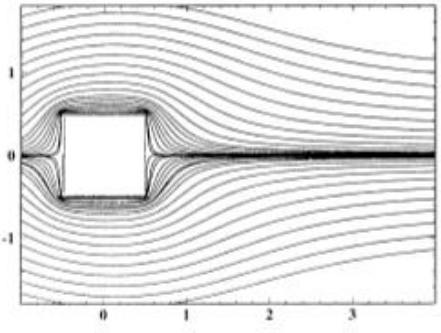

(a) This work (b) Breuer

Fig 5.3.9 Streamline at *Re* = 1

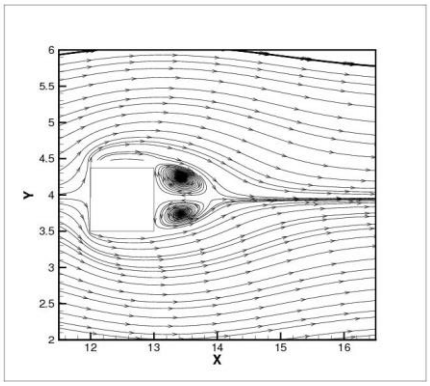

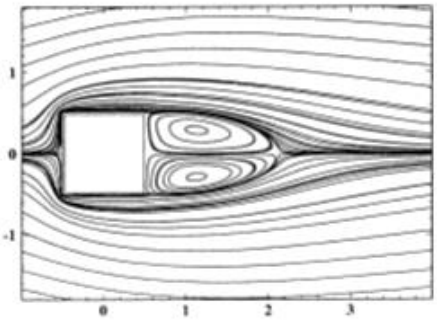

(a) This work (b) Breuer

Fig 5.3.10 Streamline at *Re* = 30

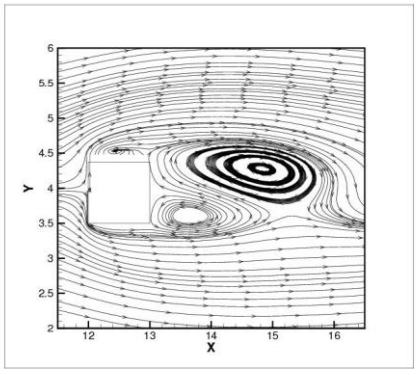

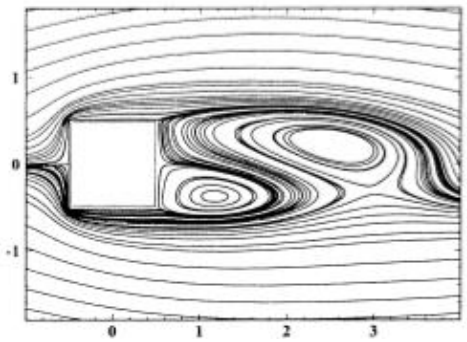

(a) This work (b) Breuer

Fig 5.3.11 Stream line at *Re* = 60

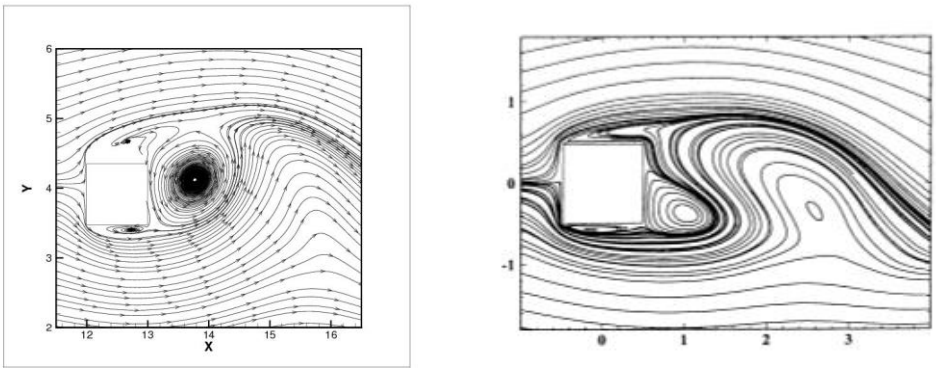

(a) This work (b) Breuer

Fig 5.3.12 Stream line at *Re* = 200

Fig 5.3.13 – Fig 5.3.15 show the contours of pressure and velocities at different *Re*, which is clearly demonstrate the details of the fluid past square cylinder.

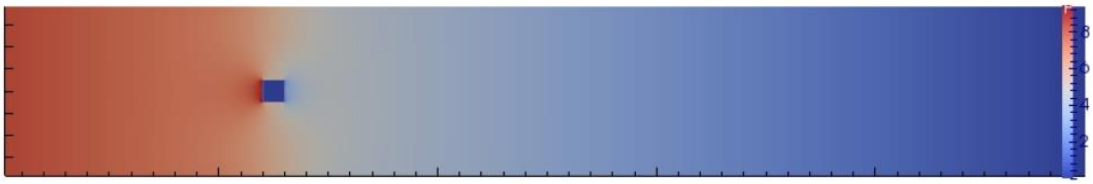

(a) *Re* = 1

(b) *Re* = 5

(c) *Re* = 60

(d) *Re* = 100

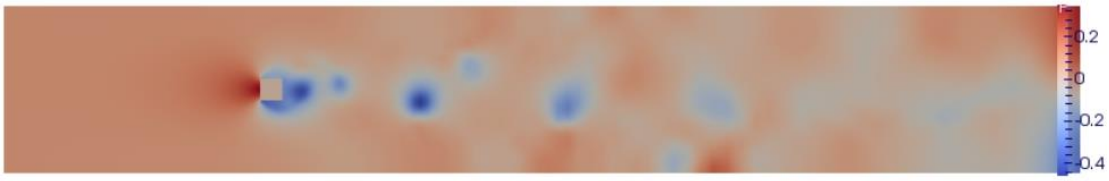

(e) *Re* = 165

(f) *Re* = 200

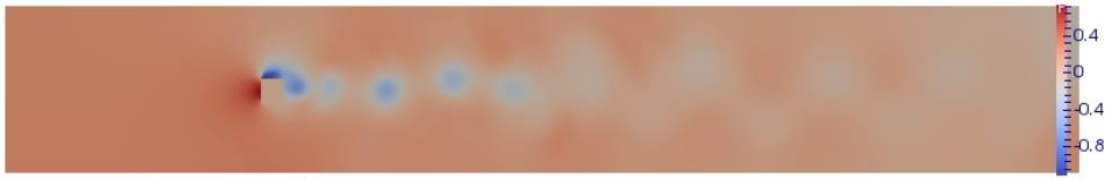

(g) *Re* = 250

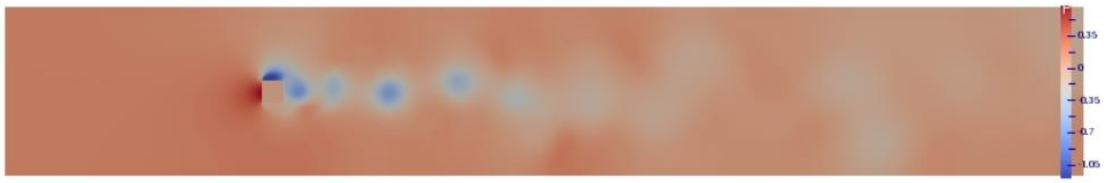

(h) *Re* = 300

Fig 5.3.13 Contours of pressure at different *Re*

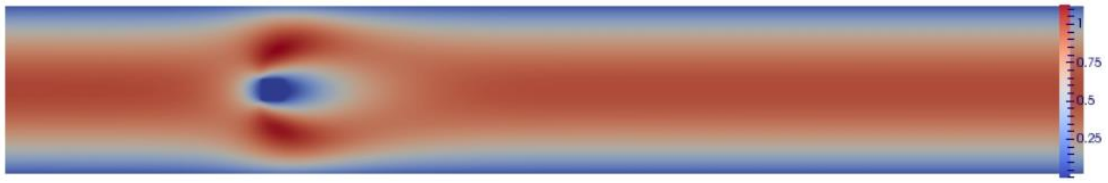

(a) *Re* = 1

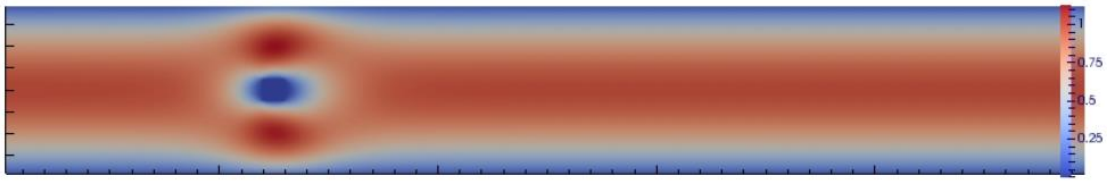

(b) *Re* = 5

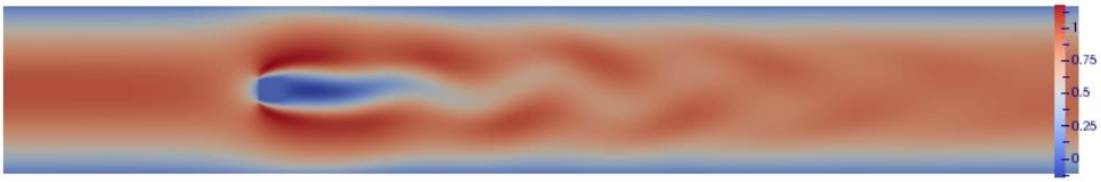

(c) *Re* = 60

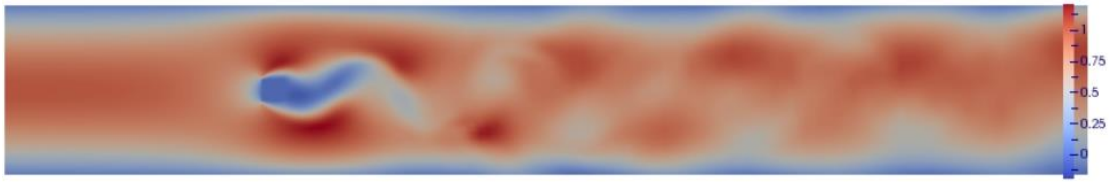

(d) *Re* = 100

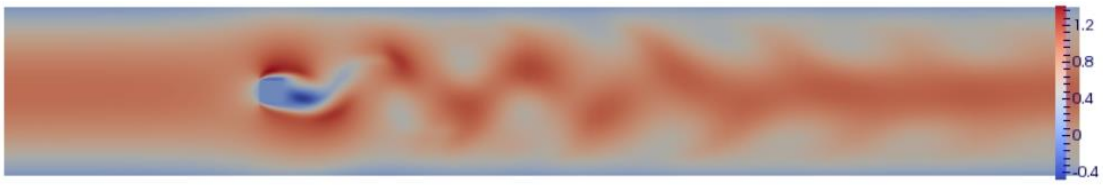

(e) *Re* = 165

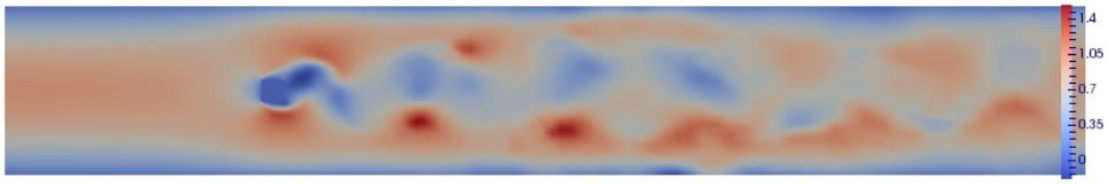

(f) *Re* = 200

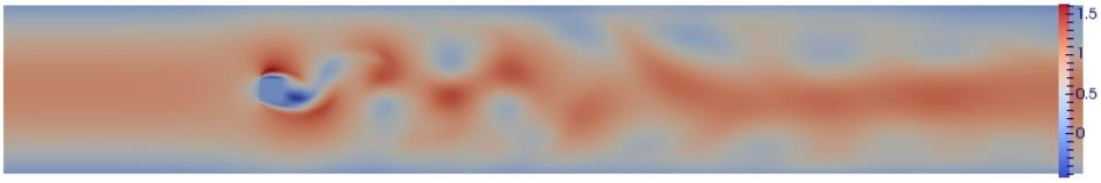

(g) *Re* = 250

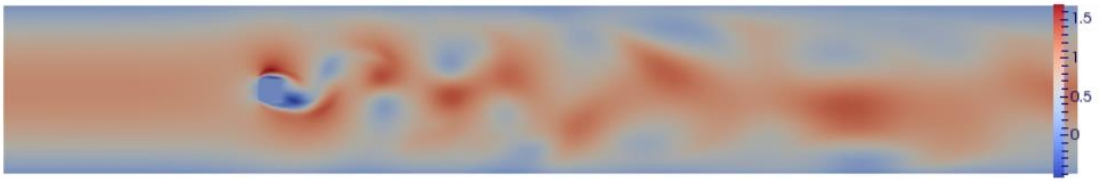

(h) *Re* = 300

Fig 5.3.14 Contours of *Ux* at different *Re*

(a) *Re* = 1

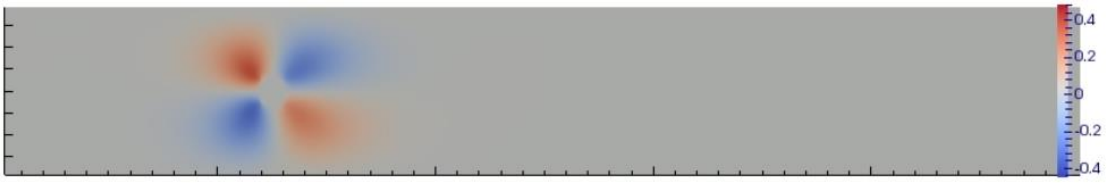

(b) *Re* = 5

(c) *Re* = 60

(d) *Re* = 100

(e) *Re* = 165

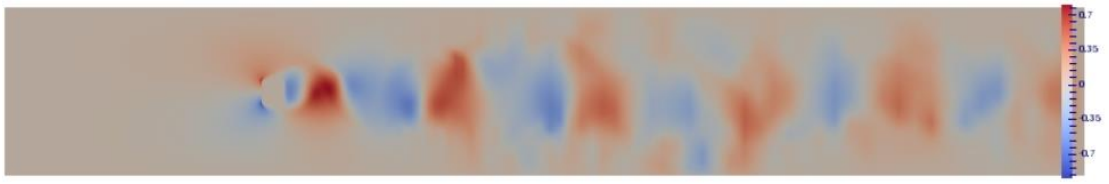

(f) *Re* = 200

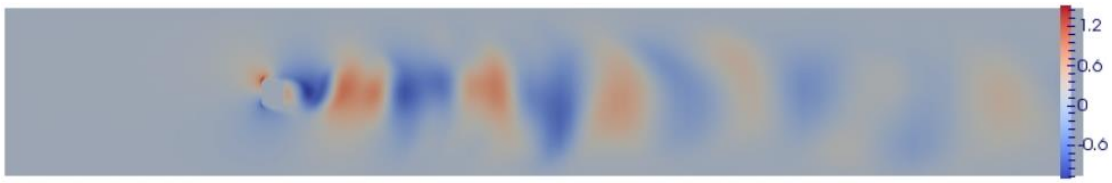

(g) *Re* = 265

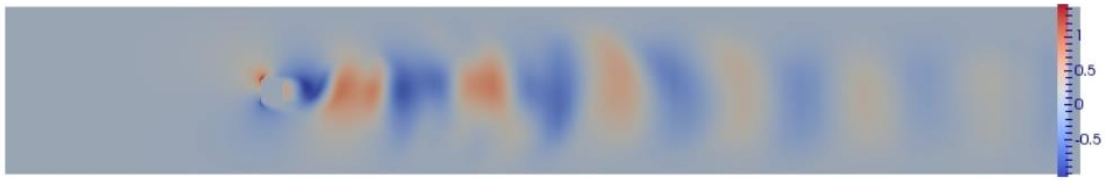

(h) *Re* = 300

Fig 5.3.15 Contours of *Uy* at different *Re*

Chapter 6: Falling film absorption process simulation

6.1 Problem description

6.1.1 Absorption phenomenon

In this chapter, an absorption process will be investigated here as a simulation of the process occurring in the absorber in a absorption chiller. The main idea is making a falling film along the vertical plate where the absorption process will occur. The concentrated solution will absorb water vapor on the interface with vapor, meanwhile the dilution process heat will be effused to the refrigerant.

With the possibilities of varies kinds of working fluids [27,28], the most conventional absorption working fluid are ammonia water (NH_3-H_2O) and Lithium Bromide solution, and they all have their own advantages. The fundamental requirements for a refrigerant – absorbent mixture are:

a wide range of miscibility within the operating pressure and temperature conditions in absorber.

b wide range of immiscibility during generator process

c mixture should be chemically stable, non-toxic, and non-explosive

The working fluid NH_3-H_2O has been widely used since the refrigerant NH_3 and absorbent H_2O are both highly stable for a wide range of operating temperature and pressure. NH3 has a high latent heat of vaporization, which is necessary for an high efficiency system. Also, as its freezing point is $-77\,^{\circ}C$, NH_3 could be used in applications of refrigeration at low temperature. But NH_3 is extreme volatile which lead to a high stable operation pressure, and toxic, corrosive which may cause corrosion in the copper tube and alloy inside it. On the other hand, LiBr-H_2O is almost non-volatile and has a high latent heat, therefore low temperature application may employ LiBr-H_2O. But using water as the refrigerant leads to a evaporator temperature limit at $0\,^{\circ}C$, in which the system should be operated at vacuum condition. Besides, aqueous LiBr at high concentration may also cause corrosion and tend to crystallize, and it is also expansive.

The working fluid in this case will be LiBr-H_2O, and will be operated under vacuum condition.

6.1.2 Falling film problem

As showed in the Fig 6.1, a falling film is a descent liquid flow that drove only by gravity. In this case, the liquid is aqueous lithium bromide with certain inlet properties, in which heat and mass transfer will be investigated. Basics hypothesis will be considered [28]:

a. The flow is a fully developed smooth laminar flow
b. The fluid properties are constant and not varying with temperature and concentration
c. The mass rate of vapor absorbed is very small compared to the solution flow rate such that the film thickness and flow velocities can be treated as constant.
d. Heat transfer in the vapor phase is negligible
e. Vapor pressure equilibrium exists between the vapor and liquid at the interface
f. The Peclet numbers are large enough such that the diffusion in flow direction can be neglected
g. Diffusion thermal effects are negligible
h. The shear stress at the liquid-vapor interface is negligible

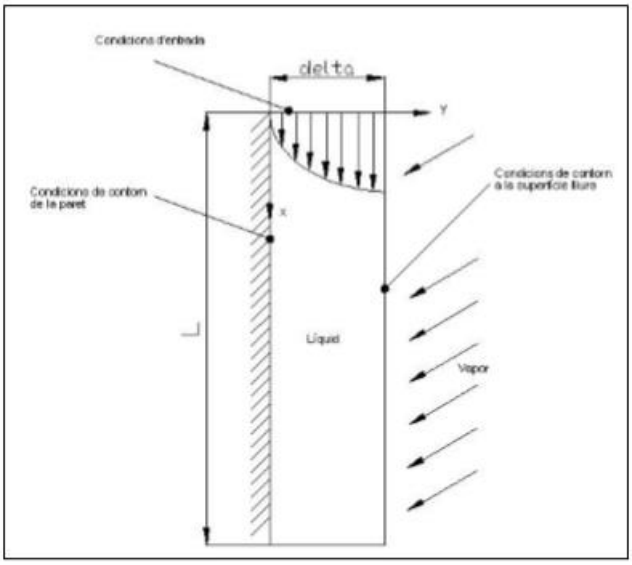

Fig 6.1.1 Liquid film descent system

6.1.3 Research purpose

This chapter will focus on heat and mass transfer in absorption processes into falling film vertical tubes. A C++ code will be built to simulate the absorption process and the result will be compared with experiment result and other's result[29,30].

Our objective is providing numerical tools with relatively low use of CPU time and experimental information for a better understanding of the absorption phenomena. As mentioned in the previous section 1.6, falling film absorption has been extensively studied, however there are some topics that are not totally understood:

6.1.4 Working fluid properties

The properties of working fluid LiBr-H_2O should be involved in the code, correlations from [31,32,33] is used here:

a. Equilibrium Conditions

$$
\begin{aligned}
&t' = (t - B)A \\
&A = -2.00755 + 0.16976X - (3.133362E-3)X^2 + (1.97668E-5)X^3 \\
&B = 321.128 - 19.322X + 0.374382X^2 - (2.0637E-3)X^3 \\
&\log P = C + D/(t' + 459.72) + E/(t' + 459.72) \\
&t' = \{-2E/(D + [D^2 - 4E(C - \log P)]^{0.5})\} - 459.72 \\
&C = 6.21147 \\
&D = -2886.373 \\
&E = -337269.46
\end{aligned}
\tag{6-2}
$$

Where $t' = \text{refregerant temperature}, {}^{\circ}F$, $t = \text{solution temperature}, {}^{\circ}F$, $X = \text{percent LiBr}$, P= absorber perssure, psia

b. Conductivity of Solution [32]

A correlation for the conductivity was extracted for the data presented in

c. $$k = 1.163(0.4945 + 0.002052t - 0.00015t^2 - 0.31c) \tag{6-3}$$

Where $k = W/(m \cdot {}^{\circ}C)$, $c = \text{concentration}$, $\text{valid range}: 30 < t < 50, 0.4 < c < 0.65$

d. Density of solution [32]

$$\rho = 1000.[(0.7086 + 1.691) - 0.0005t] \tag{6-4}$$

Where $\rho = \text{kg/m}^3$, $c = \text{concentration}$, $t = \text{temperature}, {}^{\circ}C$, $\text{Valid range}: 30 < t < 50, 0.45 < c < 0.65$

e. Diffusion Coefficient [33]

$$\begin{aligned}
&\rho = 1000.[(0.7086 + 1.691) - 0.0005t] \\
&D_{25} = 1.E-9(0.9622 + 0.435\mathrm{m}^{0.414}) \\
&\mathrm{m} = 0.01151\rho c \\
&D = [(273+t)/298][\mu_{25}/\mu_t]D_{25}
\end{aligned} \tag{6-5}$$

Where $D25 = \text{diffusion coefficient at } 25\,^{\circ}C$, $D = \text{diffusion coefficient at } t$, $\rho = \mathrm{kg/m^3}$, $t = \text{temperature},^{\circ}C$, $\mu_{25} = \text{viscosity at } 25\,^{\circ}C$, $\mu_t = vis\cos ity\ at\ t$

f. Enthalpy of solutions[31]

$$\begin{aligned}
&\mathrm{h} = a' + b't2 + c't3 \\
&\mathrm{a}' = 2326.(\mathrm{A} + 32.\mathrm{B} + 1024.\mathrm{C}) \\
&\mathrm{b}' = 2326.(1.8\mathrm{B} + 115.2\mathrm{C}) \\
&\mathrm{c}' = 2326.(3.24\mathrm{C}) \\
&\mathrm{A} = 1015.07 + 79.5387X - 2.358016X^2 \\
&+0.03031583X^3 - (1.400261E-4)X^4 \\
&\mathrm{B} = 4.68108 - (3.037766E-1)X \\
&+(8.44845E-3)X^2 - (1.047721E-4)X^3 + (4.80097E-7)X^4 \\
&\mathrm{C} = -4.9107\mathrm{E}-3 + (3.83184\mathrm{E}-4)X \\
&-(1.078963E-5)X^2 + (1.3152E-7)X^3 - (5.897E-10)X^4
\end{aligned} \tag{6-6}$$

Where $t = \text{temperature},^{\circ}C$, $X = \text{percent LiBr}$, $\mathrm{h} = \text{enthalpy,J/kg}$

g. Heat of Absorption[32]

$$\begin{aligned}
&\mathrm{a} = 2.5124\mathrm{E}6 - (483.3 + 4177t) \\
&+4187(-202.21 + 1398.47c - 2465.14c^2 + 1410.1c^3)
\end{aligned} \tag{6-7}$$

Where $c = \text{concentration}$, $t = \text{temperature},^{\circ}C$, $\mathrm{a} = \text{heat of absorption,J/kg}$,

valid range: 30<t<50,0.4<c<0.65

h. Viscosity of Solution[32]

$$\mu = 1.\mathrm{E}-3[1. + 0.1859/(1.22t)\exp(13.078c)] \tag{6-8}$$

where $c = \text{concentration}$, $t = \text{temperature},^{\circ}C$,

valid range: 30<t<50,0.45<c<0.65

6.2 Control equation and boundary condition

6.2.1 Govering equation

The control equation of this problem is consistent with equation (2-12) with Table 2.1, in term of energy and concentration, with the hypothesis mentioned above, the equations could be expressed as:

$$u\frac{\partial T}{\partial x}=\alpha\frac{\partial^2 T}{\partial y^2} \tag{6-9}$$

$$u\frac{\partial C}{\partial x}=D\frac{\partial^2 C}{\partial y^2} \tag{6-10}$$

6.2.2 Boundary conditions

The inlet solution is considered as a fully developed laminar flow, according to the Newton viscosity law, the shear force is as:

$$\tau=\mu\frac{du}{dy} \tag{6-11}$$

When integrated in the y direction the equation will turn into:

$$v_x(y)=\frac{\rho g\delta^2}{\mu}[\frac{y}{\delta}-\frac{1}{2}(\frac{y}{\delta})^2] \tag{6-12}$$

Where δ represents the thickness of the aqueous film $\delta=(\frac{3\mu}{\rho^2 g})^{\frac{1}{3}}$.

In the inlet part of the film, the solution remains at temperature and concentration at T_{in},C_{in} with a mass flow rate $\dot{m}$.

The wall on the left is considered as impermeable $\frac{\partial C}{\partial y}=0$ and isothermal at T_w.

The right boundary is the interface of solution and water vapor. When the solution on the right boundary reach equilibrium condition the temperature and concentration will satisfy

$$-\lambda\frac{\partial T}{\partial y}=\rho D\frac{\partial C}{\partial y}Ha \tag{6-13}$$

The system will work in a specific pressure, where the concentration satifies $C=C_{equil}(T,P_v)$ [34].

6.3 Discretization process

As mentioned in Chapter 3, the discretization of this case will also require FVM but with a little difference since the parabolic structure of the governing equations. Though the equation (6-9)(6-10) are 2 dimensional, it could also be introduced to a

1D discretization with a transient form. The line above is considered as the past time step and will only appear in the source term.

The Crank-Nicholson.[35] method is employed here to get suitable coefficient in the discretization equation. In order to get a better value at point (*i*,*j*), the value of adjacent nodes is take as a mean from current and previous time step, and the time step here means the vertical direction step size.

6.3.1 Discretization of energy equation

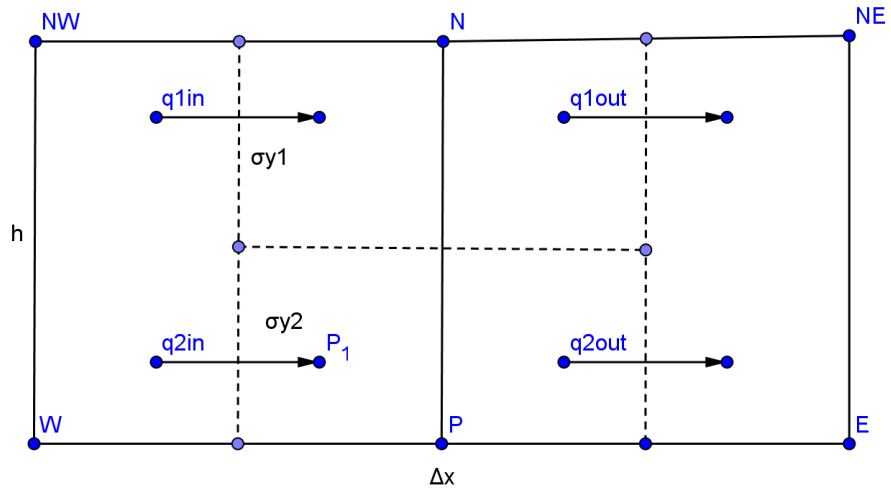

Fig 6.2 A control volume of 6 points system in falling film

As showed in Fig 6.2, the energy balance could be obtained as:

$$\int_w -\lambda\frac{\partial T}{\partial x}\mathrm{d}y+\int_e -\lambda\frac{\partial T}{\partial x}\mathrm{d}y+\int_V \rho C_p\frac{\partial T}{\partial t}\mathrm{d}x\mathrm{d}y+\int_V S_P\mathrm{d}x\mathrm{d}y=0 \qquad (6\text{-}14)$$

$$q_{1\_in}+q_{2\_in}-q_{1\_out}-q_{2\_out}+S=0 \qquad (6\text{-}15)$$

Where

$$q_{1\_in}=\lambda\frac{T_N-T_{WN}}{\delta_x^w}\delta_y^1,\ q_{1\_out}=\lambda\frac{T_{EN}-T_N}{\delta_x^e}\delta_y^1,\ q_{2\_in}=\lambda\frac{T_P-T_W}{\delta_x^w}\delta_y^2,\ q_{2\_out}=\lambda\frac{T_E-T_P}{\delta_x^e}\delta_y^2,$$

$$S=Uy\rho C_p\frac{T_N-T_P}{\delta_y^n}\Delta x$$

The final discretization equation is:

$$aP*T_P=aE*T_E+aW*T_W+b \qquad (6\text{-}16)$$

Where $aE = \lambda \frac{\delta y_2}{\delta_x^w}$, $aW = \lambda \frac{\delta y_2}{\delta_x^e}$, $aP = aE + aW + \rho C_p Uy \frac{\Delta x}{\delta_y^n}$,

$b = \lambda \frac{\delta y_1}{\delta_x^w} T_N - \lambda \frac{\delta y_1}{\delta_x^w} T_{WN} + \lambda \frac{\delta y_1}{\delta_x^e} T_N - \lambda \frac{\delta y_1}{\delta_x^e} T_{EN} + \rho C_p Uy \frac{\Delta x}{\delta_y^n} T_N$, Δx is distance of the node face, δy_1 represents the distance from node point to north face while δy_2 represents the south part.

On the boundaries,

Top: the temperature of inlet is fixed, so $aE = 0$, $aW = 0$, $aP = 1$, $b = T_{in.}$

Bot: free outlet condition is employed here, and the coefficients will be the same.

Left: left side of the fluid is connected with the wall, and the temperature is set as the wall temperature, so $aE = 0$, $aW = 0$, $aP = 1$, $b = T_{\text{wall.}}$

Right: on the right boundary the temperature will be calculated from the equilibrium concentration from Scant method, so it is also considered as fix as $aE = 0$, $aW = 0$, $aP = 1$, $b = T$.

6.3.2 Discretization of specie equation

The discretization of specie equation is similar with the one of energy equation since they share the same transport equation. The same method was used here, hence the result form is as Eq(6-8) but with different coefficients:

$aE = D \frac{\delta y_2}{\delta_x^w}$, $aW = D \frac{\delta y_2}{\delta_x^e}$, $aP = aE + aW + Uy \frac{\Delta x}{\delta_y^n}$,

$b = D \frac{\delta y_1}{\delta_x^w} T_N - D \frac{\delta y_1}{\delta_x^w} T_{WN} + D \frac{\delta y_1}{\delta_x^e} T_N - D \frac{\delta y_1}{\delta_x^e} T_{EN} + Uy \frac{\Delta x}{\delta_y^n}$

Top: the concentration of inlet is fixed, so $aE = 0$, $aW = 0$, $aP = 1$, $b = C_{in.}$

Bot: free outlet condition is employed here, and the coefficients will be the same.

Left: left side of the fluid is connected with impermeable wall, the concentration will remain at 0, so $aE = 0$, $aW = 0$, $aP = 1$, $b = 0$. Besides, the coefficients of fluid part connected to the wall should also be modified as $aW = 0$, the rest is the same.

Right: on the right boundary the concentration will be hypothesized and calculated from Secant method, so it is also considered as fixed as $aE = 0$, $aW = 0$, $aP = 1$, $b = T$.

6.4 solve procedure

6.4.1 Mesh

As showed in Eq (6-9) (6-10), the coefficient in the transport equation is minute, and the height, thickness of the solution is not at the same magnitude (Re = 4 H = 1.0, δ is around 2E-4), which means the heat and mass transfer will take place in only a small portion of the length and height. Therefore, a hyperbolic mesh should be employed to investigate the performance in the beginning after the inlet flow. The hyper factor in the vertical direction should be around 5.0 and concentrated to the inlet direction, while in horizontal direction symmetric form is at factor at around 2.0.

The mesh here employs (3-1) at concentration to top and symmetry, as showed in Fig 6.3 Fig 6.4, due to the thickness scale only a small part of mesh is demonstrated.

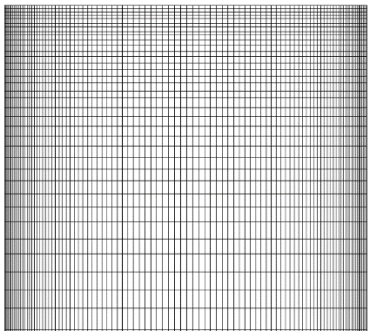

Fig 6.4.1 Mesh of falling film problem

6.4.2 Secant method

In equation (6-5), the interface of solution and vapor could reach an equilibrium condition at a specific pressure, which is very sensible to all the variables. In order to solve this problem and save CPUs, scant method is used here.

Firstly, we assume the concentration C_0, C_1 of the solution on the interface, which accordingly could result the temperature. Through the function of residual:

$$f = \lambda \frac{\partial T}{\partial y} + \rho D H_a \frac{\partial C}{\partial y} \tag{6-17}$$

we could get T_0,T_1 and $f(x_0)$,$f(x_1)$, then

$$C_2 = C_0 - \frac{C_1 - C_0}{f(C_1) - f(C_0)} f(C_0) \tag{6-18}$$

new concentration will be acquired, this process will finally lead to $f \to 0$. Besides, a relaxion factor $f_r(0,1)$ should be involved here dur to the drastic change of f, and usually the relax factor should be smaller with a finer mesh.

$$C_2 = C_1 + f_r(C_1 - C_0) \tag{6-19}$$

6.4.3 Solver

This case is 2D in general, but according to the hypothesis the problem could be divided to a set of 1D problems. A TDMA solver could be used to solve the problem which could both acquire reasonable result and save computational time. Besides, a relaxation factor is used when the variable is evaluated in the algorithm due to the extreme sensible mesh.

6.5 Algorithm of descent film resolution

6.5.1 Introduction

Fig 6.5.1 shows the simplified algorithm, in which concentration will be calculated until it and the corresponding temperature could satisfy the Eq. (6-17). The variables are calculated line by line, and the variables of the upper line is considered as variables of old time step and will appear in the source term.

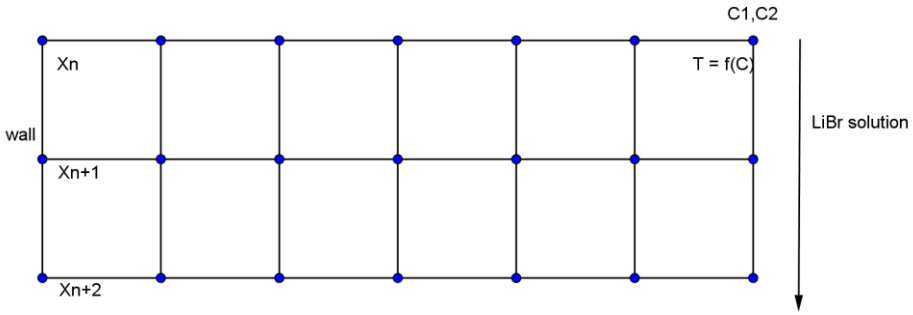

Fig 6.5.1 Algorithm of descent film resolution

6.5.2 Algorithm

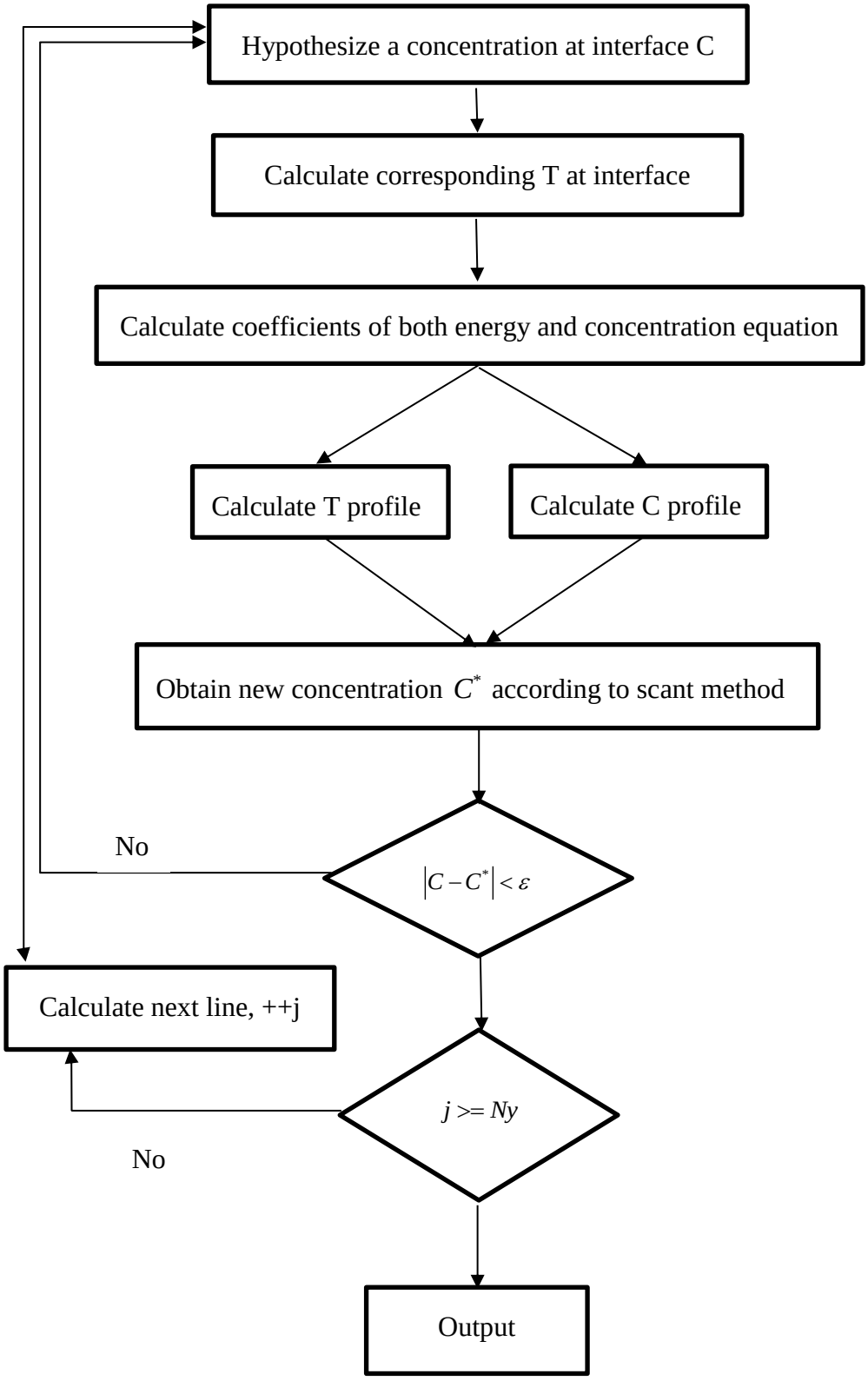

Fig 6.5.2 Flow chart of algorithm of falling film

6.6 Numerical result

6.6.1 Introduction

Result of numerical simulation of falling film absorption process at inlet condition

$T_{\mathrm{w}} = 35\,^{\circ}\mathrm{C}$
$T_{\mathrm{in}} = 44.44\,^{\circ}\mathrm{C}$
$C_{\mathrm{in}} = 0.6(\mathrm{LiBr})$
$P = 7.02\mathrm{mmHg}$

6.6.2 Result

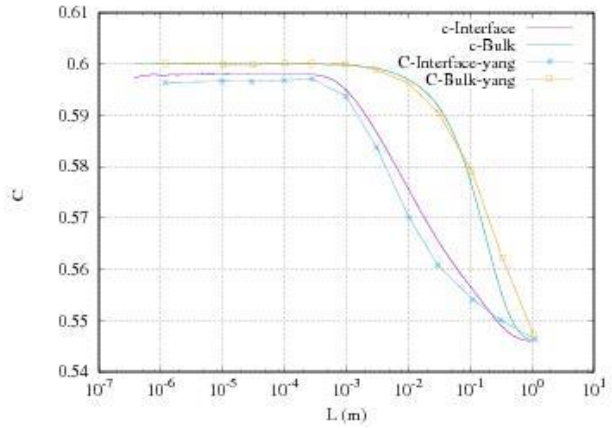

Fig 6.5.3 Numerical result of concentration compared with result of Yang

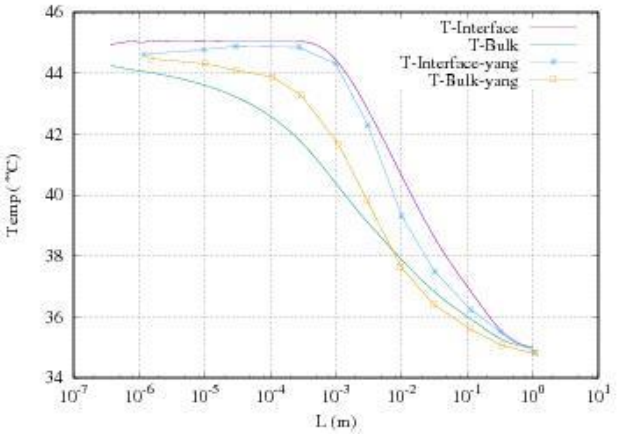

Fig 6.5.3 Numerical result of concentration compared with result of Yang

The code was built in a similar way with code in the reference, though the thermophysical properties and interface equilibrium condition correlation may not be the same. The discrepancy of the result is acceptable due to the high sensitive result.

6.6.3 Definition of heat and mass transfer coefficient

The mass absorption of water vapor rate $\dot{M}_{abs}$ is calculated by[36]

$$\dot{M}_{abs} = \dot{M}_{\text{solution\_out}} - \dot{M}_{\text{solution\_in}} \tag{6-20}$$

Where $\dot{M}_{\text{solution\_out}}, \dot{M}_{\text{solution\_in}}$ represent the mass flow rate of solution at inlet and outlet. In the system the mass of LiBr is constant so $\dot{M}_{\text{solution\_out}} * C_{\text{out}} = \dot{M}_{\text{solution\_in}} * C_{\text{in}}$, thus we could obtain

$$\dot{M}_{\text{abs}} = \dot{M}_{\text{solution\_out}} * (1 - C_{\text{out}} / C_{\text{in}}) \tag{6-21}$$

Respectively, the heat transfer to the cooling water $\dot{Q}$ in the absorber is

$$\dot{Q} = \dot{M}_{\text{solution\_in}} * h_{\text{in}} - \dot{M}_{\text{solution\_out}} * h_{\text{out}} - \dot{M}_{abs} * H_{\text{a}} \tag{6-22}$$

Where $h_{\text{in}}, h_{\text{out}}$ is the enthalpy of the solution corresponding to the location, and H_{a} is absorption heat of LiBr solution.

6.6.4 Film heat transfer coefficient

In the general form of heat transfer [37]

$$\dot{Q} = UA(T_{\text{eq}} - T_{\text{c}}) \tag{6-23}$$

Where *A* is outside surface area of stainless tube

U is overall heat transfer coefficient

T_{c} is the average temperature of cooling water in $^{\circ}\text{C}$

T_{eq} is the equilibrium temperature at the solution inlet temperature and absorber pressure.

$$\frac{1}{U} = \frac{1}{h_{\text{f}}} + \frac{r_{\text{n}}}{k_{\text{w}}} \ln \frac{r_{\text{n}}}{r_{\text{l}}} + \frac{r_{\text{n}}}{r_{\text{l}}} \frac{1}{h_{\text{c}}} \tag{6-24}$$

Where h_{f} is the film heat transfer coefficient

k_{w} is the thermal conductivity of the metal tube 14.9 $\text{W/m} \cdot \text{K}$[38]

$r_{\text{l}}, r_{\text{o}}$ is the inside and outside radius of the tube

h_{c} is the heat transfer coefficient of cooling water[39]

$$h_c = 150(1+0.011T_c)\frac{V^{0.8}}{d^{0.2}} \tag{6-24}$$

$$h_c = 2140(1+0.011(32+1.8T_c)\dot{M}_c^{0.8})\text{Fc}$$
$$\text{Fc}=1+\frac{1.4}{L/d} \tag{6-25}$$

Where h_c in $\text{W}/\text{m}^2\cdot^\circ\text{C}$

$\dot{M}_c$ is mass flow rate of cooling water, kg/sec

d is the inside diameter of the tube

T_c is the average temperature of cooling water in $^\circ\text{C}$

Then h_f is

$$h_f = \frac{l}{\frac{1}{U}-\frac{r_n}{k_w}\ln\frac{r_n}{r_1}-\frac{r_n}{r_1}\frac{1}{h_c}} \tag{6-26}$$

6.6.5 Mass transfer coefficient

The mass transfer coefficient could be defined as below

$$\dot{M}_{abs} = \rho h_m A[C_{solution\_in} - C_{eq}(T_c, P_v)] \tag{6-27}$$

Where ρ is density of LiBr solution

h_m is mass transfer coefficient

A is total effective surface area

C_{eq} is the equilibrium concentration of the solution at absorber pressure and cooling water temperature

In summary, the maximum possible driving potential is utilized in the system, which means the equilibrium condition at an infinite contact length and steady state, hence the operating system only depends on the inlet condition. Besides, though the mean cooling water temperature depends on both inlet and outlet condition, it can be estimated as inlet temperature plus 0.15°C, because the temperature difference is generally less than 0.4. It should be noticed that the wall is evaporatively cooled, T_c is replaced by the ambient wet-bulb temperature which is a known quantity.

6.7 experimental apparatus

6.7.1 Scope of apparatus setup

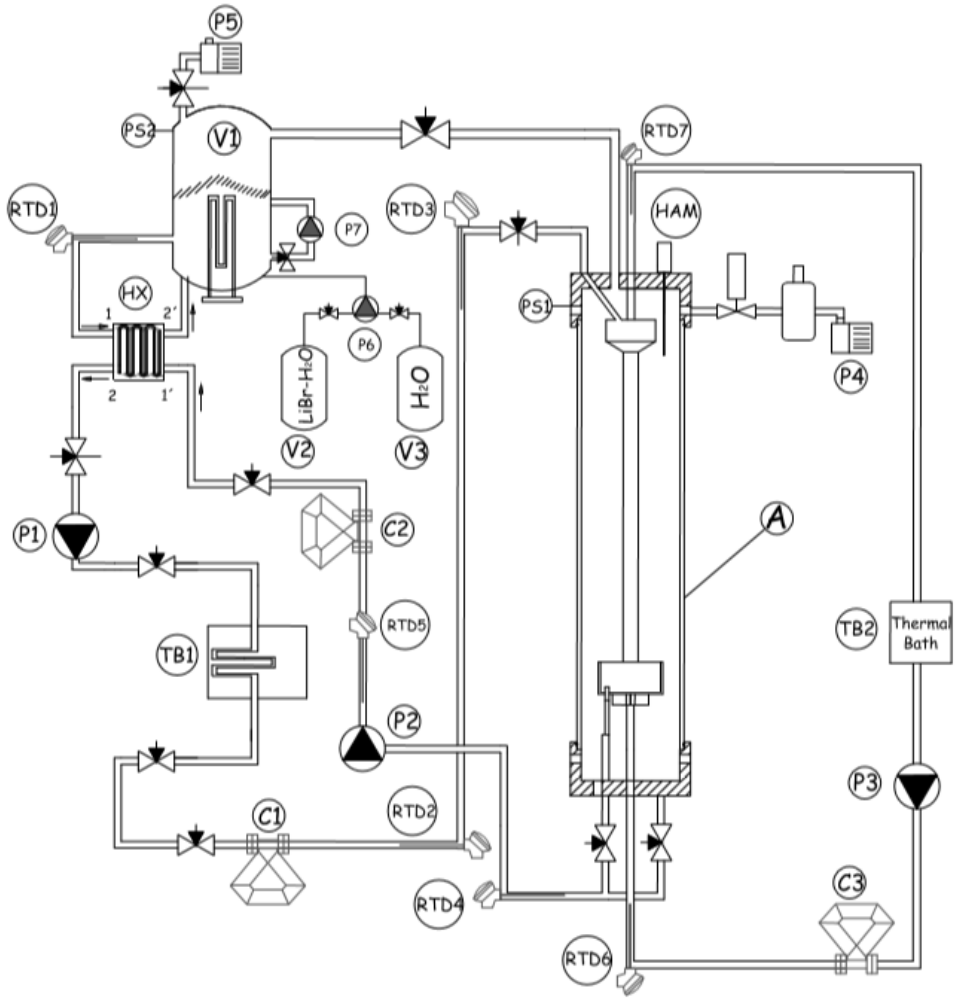

Fig 6.6.1 Figure of experimental apparatus of falling film

The commercial characteristics and specifications of the experimental set-up are:

a. Two magnetically coupled gear pumps of variable velocity (Cole-Parmer E-7401145), with the following specifications:
   - Stainless steel.
   - 0.32−8.00 l/min of flow.
   - Connection to the process 1/4” NPT.
   - 230 VAC 50/60 Hz

b. Two vacuum pump (Telstar model 2G-9 and 2G-6), specifications:
   - 9 m3/h of volumetric flow.

- 8·10−4 mbar of vacuum limit.

c. One thermostatic bath Haake model N3, Type 001−5722.
   - 3000 W of heating capacity.
   - Temperature Range:5 oC ÷80oC

d. One thermostatic bath Huber model CC −245Wl.
   - 3000 W of heating capacity.
   - Temperature range −45÷200 oC.

e. Two mass flow meters and densimeters (Micro Motion Elite) reference CMF025M300NB.
   - Accuracy: ± 0.15 % of reading in the mass flow
   - 0.0005g/cm3 in density with the transmitters Micro Motion Elite reference RFT9739E4EBB

f. An absolute pressure sensor (Rosemount 3051S, EMERSON).
   - Range 0 to 2000 Pa.
   - Accuracy: 0.125 % of reading.

g. An absolute pressure sensor (Rosemount 3051S, EMERSON).
   - Range 0 to 10000 Pa.
   - Accuracy: 0.125 % of reading.

h. Seven temperature probes PT100. Calibrated in order to correct possible bias in the readings.
   - Class B.
   - accuracy; 1/10 DIN (±0.03◦C).
   - Material: Pyro-Alloy c

i. An optical Oxygen and temperature sensor.
   - Measurement principle: oxygen dependent luminescence (Hamilton).
   - Temperature range -10 to 130 ^{o}C.

6.7.2 Vacuum requirements

Typical pressures in a single effect aqueous LiBr absorption chiller are sub-atmospheric. This experimental apparatus will be operated at pressure 7.02 mmHg. This pressure level is not particular low but could be very sensible to the air leak, since air may degrade the absorption performance and cause corrosion.

In order to ensure the hermetic ability of the system, the main elements are evaluated individually and then as a whole. The detection procedure is as below:

a. The component should be connected to a cold trap and vacuum pump, and a Pirani gauge is connected to the component to evaluate the pressure instantaneously.
b. When the system is set, open the vacuum pump and wait till the pressure reach the vacuum limit, depends on the volume of the component this could last a day. The leak rate F of the system should be under 1E-5 $\mathrm{Pa \cdot m^3 \cdot s^{-1}}$ and is calculated as:

$$F = \frac{V \Delta p}{\Delta t} \tag{6-9}$$

where V is the volume of the system to be evaluated, Δt is the time of two measurements, Δp is the pressure difference between Δt.

c. Next, open the pump another time till the limit, and then turn the valve and pour liquid nitrogen to the cold trap. With the liquid nitrogen, the molecular liquid will be captured in the trap resulting a dry leak rate of the system.

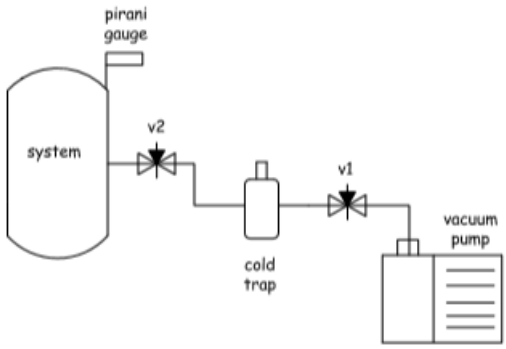

Fig 6.6.2 Schematic sketch of the leak test system

6.7.3 Leaks and detect method

Once the system could not satisfy the hermetic requirement, there are two possibilities. One is that there is a micro leak in the system, which is difficult to find out, the other mean there is virtual leak in the system.

To find a leak is not an easy issue, common procedures depend on the leak rate are as below:

a. The vacuum of the system could not reach below 1e-1mbar.

   The system could be injected Helium and reach a pressure at 5 Bar, then use He detector to scan the system.

   The system could also be submerged to water after inject compress air or He. Stare at the water and trace the bubble.

   Soup water could also be painted to the surface, and at the leak point the foam will pile up.

   These kinds of leak usually take place at joint, fittings.

b. The leak rate of the system is above 1e-5.

   Micro leaks below 1e-5 could be extremely difficult to find and techniques above may not help, so the best way is either using a commercial leak detector or a mass spectrometry.

   A virtual leak is a source of gas that's physically trapped within the source system with only a small, very low conductance of the path from the trapped pocket of gas to the system.

   A rudimentary technique is keep the system in its maximum possible vacuum level, then apply soup water to suspicious leak areas (fitting, joints, etc.) the Pirani's lecture gives a lower pressure due to the water molecule blocks the leaks, and also, the pressure may increase suddenly as the molecular water enter the vacuum system. Liquid nitrogen could reduce the affluence of virtual leak but could not eradicate it, sometimes make the pump for a longer time could also decrease the virtual leak. Patience is the key point to deal with virtual leaks as they are virtual, they may change at any time. Generally, during vacuum test, instantly after the valve connected to the pump is turned off, the leak in the first 5 minutes should be the same with the next hours, if there is a big difference, it may drive to virtual leak. In conclusion, vacuum is an essential condition imposed by the properties of the working fluid though it is not an easy topic. Patience and methodology are critical factor in order to achieve acceptable vacuum levels. In the case of this experimental apparatus, the whole system´s leak rate is around $1.54 \cdot 10^{-5}$ $Pa \cdot m^3 \cdot s^{-1}$, which is acceptable in the case.

6.8 Procedure of operation

Once the experimental unit is ready to work, it is necessary to establish a procedure for operating properly the experimental apparatus.

a. The vacuum pumps (P4) and (P5) should be left turned on a whole night before the working day in order to acquire the possible minimum pressure.
b. The absorber and the generator must be isolated hydraulically one to each other before starting.
c. Turn on the PID which controls heat sources in the generator. The generator was left running for a period until the pressure reaches a desired value.
d. The thermal baths (TB1) and (TB2) are turned on. (TB2) is set with the inlet coolant temperature, while (TB1) is set about 10°C below the theoretical inlet solution temperature saturation conditions.
e. Pumps (P1) and (P2) are turned on, and vapor circuit is opened. Then aqueous solution starts to flow and the falling film is formed at the same time that vapor emigrates from generator to the absorber. At this point it is useful to monitoring the following variables: inlet and outlet temperatures for both the primary solution circuit and the coolant fluid, the inlet and outlet solution densities, generator and absorption pressures and inlet solution mass flow.
f. By using the inlet solution temperature and density, the inlet concentration is calculated cin. If cin is not the desired then it can be adjusted using (P6) and either (V2) or (V3).
g. The PID which drives the generation should be adjusted if needed. As the absorption pressure increases Pabs the inlet solution temperature needs to be readjusted using (TB1). It is important to keep inlet solution temperature close to the equilibrium during the unsteady state, in this way always there is absorption of water vapor into the falling film solution ($\rho in > \rho out$). Therefore, the system reaches the steady state easily. Once the desired absorption pressure and inlet solution temperature are reached, the inlet mass flow is adjusted.
h. We can consider that a steady-state is reached when none of the variables that govern the absorption performance show important perturbations. The Figs. 3.6, 3.7 and 3.8 shows the steady state behavior for the governing variables in a typical running

6.9 Result discuss

6.9.1 Effect of absorbent flow rate

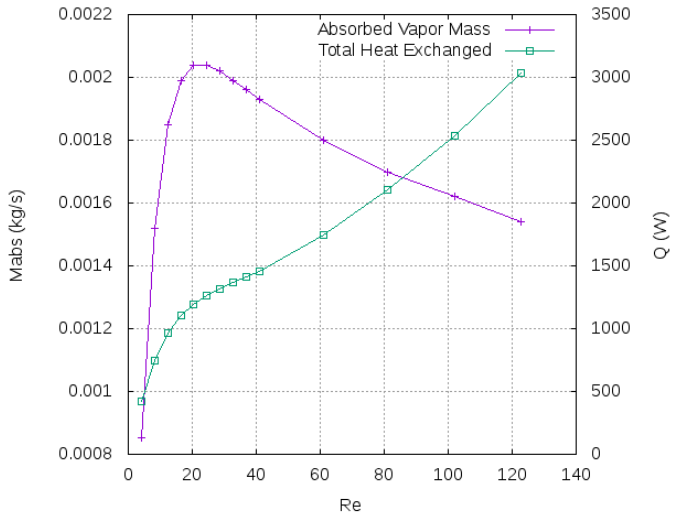

Fig 6.9.1 Vapor absorbed and heat transfer along with the *Re* number

Fig 6.9.1 shows the numerical result of vapor mass and heat transfer with smooth solution theory. The contact length at this case is 1.0m, which means the solution mass rate more than $0.01 kg \cdot m \cdot s^{-1}$ could not reach the equilibrium concentration at the cooling water temperature. The vapor mass absorbed increases and decreases due to the theoretically simultaneous heat and mass transfer while the total heat transfer will keep increasing. If infinite contact length is set, Fig 6.9.2 shows the result of essential contact length respectively to the effectiveness at 0.99 and .95. A significant of contact length ascent is required till the high *Re* number flow reaches equilibrium condition at coolant temperature.

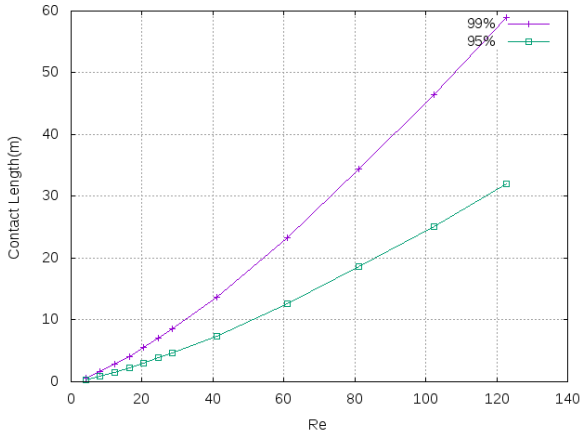

Fig 6.9.2 Essential contact length of different *Re* flow

6.9.4 Effect of cooling water and solution inlet temperature

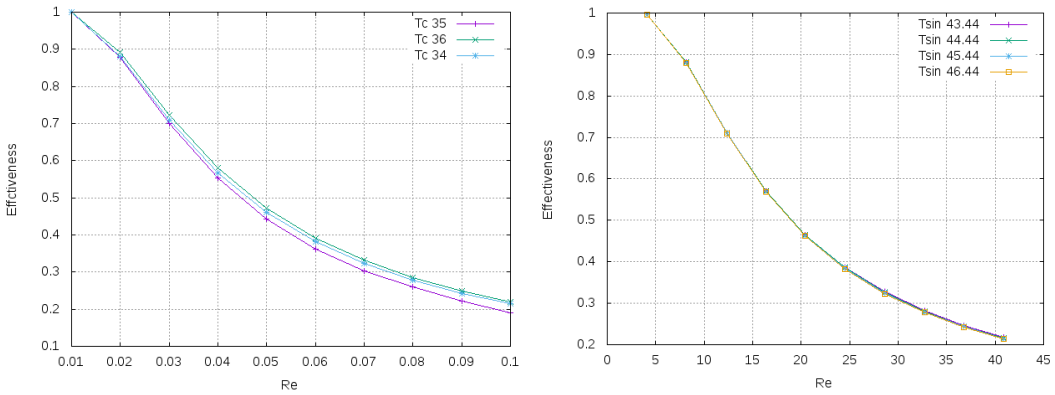

(a) Wall temperature (b) Inlet solution temperature

Fig 6.9.3 Effectiveness at different coolant temperature and inlet solution temperature

6.9.5 Effect of vapor pressure

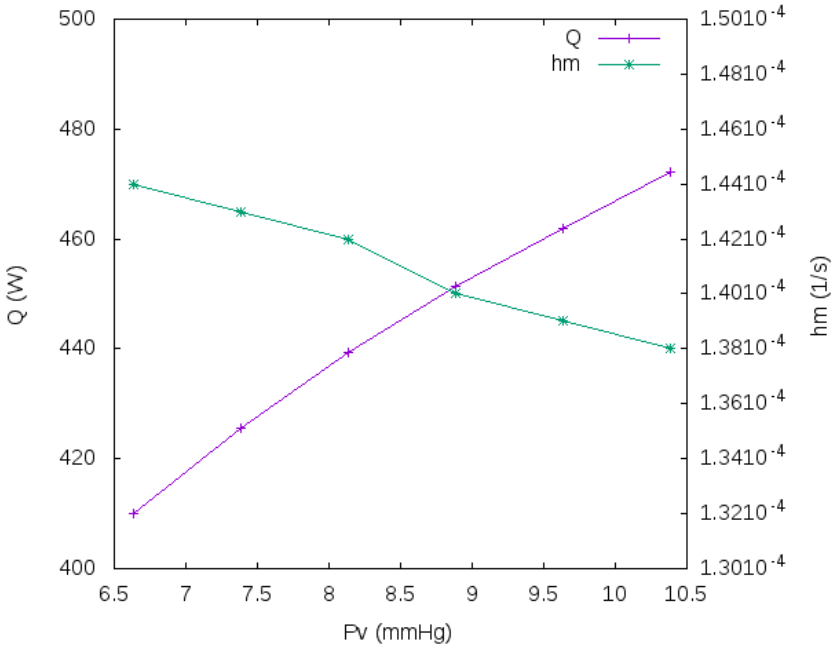

Fig 6.9.4 Total heat transfer and mass transfer coefficient at different vapor pressure

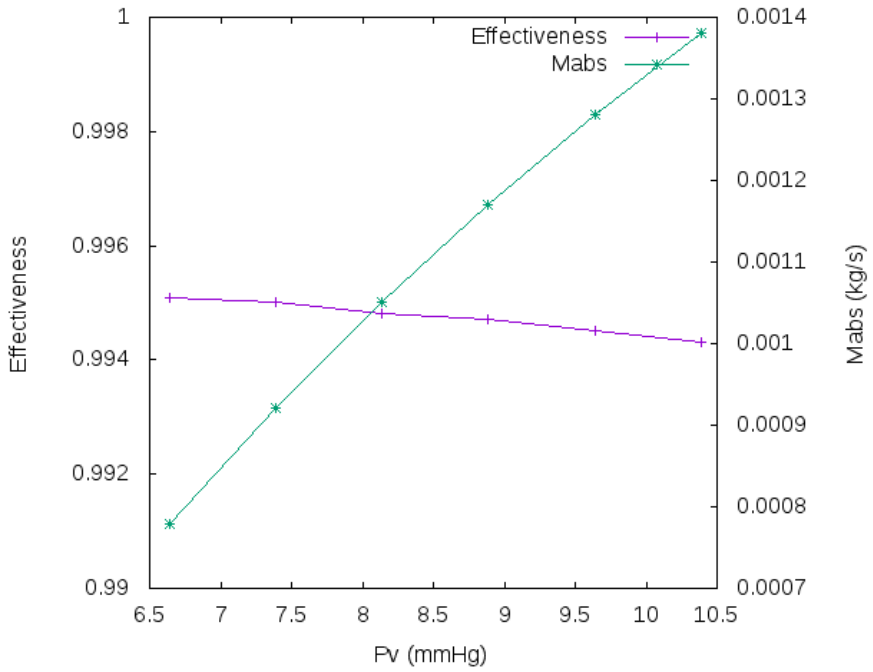

Fig 6.9.5 Effectiveness and vapor absorbed mass at different pressure

Fig 6.9.4 and 6.9.5 shows the result of coefficients at different operated pressure. In the code it is assumed that the pressure distribution is only about vapor, which means the non-absorbable gas such as air will not be considered.

Chapter 7: Conclusion and future work

This work aimed at expertise in field of fluid dynamic, heat and mass transfer problem in both simulation and experimental aspect.

In the simulation part, incompressible N-S equations and energy equation were solved and the results of them were compared with the benchmark solution in the chapters above. The simulation results match the benchmark solution generally means the computational process is correct. During the process of programming, the comprehension of heat and mass transfer and related phenomena is highly manipulated. In the part of square cylinder, vortex shedding was also investigated.

The code of absorption process revealed that in the falling film aqueous solution of LiBr, the concentration changed significantly in the entry part. In smooth solution theory, the essential contact length increases rapidly along with the *Re* number, and wall temperature, solution inlet temperature will not affect effectiveness significantly with the same contact length. With a certain length of tube, the absorbed vapor mass will increase and then decrease when the *Re* increases due to the increment of film transport velocity. In the experiment, a serial data of LiBr solution was extracted compared to the simulation result, besides, considering the wet-ability problem, low *Re* case is not conclude in the experiment part.

Due to the complexity of experiment of vacuum condition and lack of time, a full serial of experiment data could not be obtained. Part of the result is demonstrated in the Annex. The experiment will continue after this work.

Reference

[1] Departament de Máquines i Motors Térmics. Laboratori de Termotécnia i Energética. Apunts de l'assignatura de Transferéncia de Calor i de Massa, impartida a la ETSEIAT. 2005

[2] Departament Máquines i Motors Térmics. Laboratori de Termotécnia i Energética. Apunts de l'assignatura de Transferéncia de Calor i de Massa, impartida a la ETSEIAT. 2005

[3] Departament de Máquines i Motors Térmics. Laboratori de Termotécnia i Energética. Apunts de l'assignatura de Termotécnia, impartida a la ETSEIAT. 2003

[4] R.B. Bird, E.E. Stewart, and E.N. Lightfoot. Transport phenomena. John Wiley and Sons Inc., 1960

[5] Departament de Mec`anica de Fluids. Apunts de l'assignatura de Fluidot`ermia, impartida a la ETSEIAT. 2005.

[6] Darwish, M., A new high-resolution scheme based on the normalized variable formulation. Numerical Heat Transfer, Part B Fundamentals, 1993. 24(3): p. 353-371.

[7] Versteeg, H.K. and W. Malalasekera, An introduction to computational fluid dynamics: the finite volume method. 2007: Pearson Education.

[8] Alves, M., P. Oliveira, and F. Pinho, A convergent and universally bounded interpolation scheme for the treatment of advection. *International journal for numerical methods in fluids*, 2003. 41(1): p. 47-75.

[9] Kim, J., & Moin, P. (1985). Application of a fractional-step method to incompressible Navier-Stokes equations. *Journal of computational physics*, *59*(2), 308-323.

[10] Chorin, A. J. (1968). Numerical solution of the Navier-Stokes equations. *Mathematics of computation*, *22*(104), 745-762.

[11] Temam, R. (1969). Sur l'approximation de la solution des équations de Navier-Stokes par la méthode des pas fractionnaires (II). *Archive for Rational Mechanics and Analysis*, *33*(5), 377-385.

[12] Archive for Rational Mechanics and Analysis, 33:377– 385, 1969.

[13] N. N. Yanenko. The Method of Fractional Steps. Springer-Verlag, 1971.

[14] S. Xin and P. Le Quéré. Direct numerical simulations of two-dimensional chaotic natural convection in a differentially heated cavity of aspect ratio 4. *Journal of Fluid Mechanics*, 304:87–118, 1995.

[15] M. Soria, F. X. Trias, C. D. Pérez-Segarra, and A. Oliva. Direct numerical simulation of a three-dimensional natural-convection flow in a differentially heated cavity of aspect ratio 4. Numerical Heat Transfer, part A, 45:649–673, April 2004.

[16] R. W. C. P. Verstappen and A. E. P. Veldman. Symmetry-Preserving Discretization of Turbulent Flow. Journal of Computational Physics, 187:343–368, May 2003.

[17] Suhas V. Patankar. Numerical Heat Transfer and Fluid Flow. Hemisphere Publishing Corporation, McGraw-Hill Book Company, 1980.

[18] R. Courant, K. Friedrichs, and H. Lewy. ¨Uber die partiellen Differenzengleichungen der mathematischen Physik. Mathematische Annalen, 100:32–74, 1928.

[19] Erwin Simons. An efficient multi-domain approach to large eddy simulation of incompressible turbulent flows in complex geometries. PhD thesis, Von Karman Institute for Fluid Dynamics, October 2000.

[20] Ghia, U., K.N. Ghia, and C. Shin, High-Re solutions for incompressible flow using the NavierStokes equations and a multigrid method. *Journal of computational physics*, 1982. 48(3): p. 387-411

[21] DE VAHL DAVIS, G. Natural convection of air in a square cavity: a bench mark numerical solution. *International Journal for numerical methods in fluids*, 1983, vol. 3, no 3, p. 249-264.

[22] DE VAHL DAVIS, G.; JONES, I. P. Natural convection in a square cavity: a comparison exercise. *International Journal for numerical methods in fluids*, 1983, vol. 3, no 3, p. 227-248.

[23] Breuer, M., Bernsdorf, J., Zeiser, T., & Durst, F. (2000). Accurate computations of the laminar flow past a square cylinder based on two different methods: lattice-Boltzmann and finite-volume. *International journal of heat and fluid flow*, *21*(2), 186-196.)

[24] Zdravkovich, M.M., 1997. Flow Around Circular Cylinders, vol. 1: Fundamentals. Oxford University Press, New York)

[25] Shen, L., Chan, E. S., & Lin, P. (2009). Calculation of hydrodynamic forces acting on a submerged moving object using immersed boundary method. *Computers & Fluids*, *38*(3), 691-702.

[26] Klekar, K. M., & Patankar, S. V. (1992). Numerical prediction of vortex shedding behind square cylinders. *Int. J. Numer. Methods Fluids*, *14*(3), 327-341.

[27] S. Jian, F. Lin, and Z. Shingang. A review of working fluids of absorption cycles. *Progress in Energy and Combustion Science*, 16(2012):1899–1906, 2012.

[28] Srikhirin Pongsid, Aphornratana Satha, and Chungpaibulpatana Supachart. A review of absorption refrigeration technologies. *Renewable and Sustainable Energy Reviews*, 5(4):343–372, 2001

[29] Yang, R. (1987). *Heat and mass transfer in laminar wavy film absorption with the presence of nonabsorbable gases*. Arizona State Univ., Tempe (USA).

[30] Andberg, J. W. (1986). *Absorption of vapors into liquid films flowing over cooled horizontal tubes*. Texas Univ., Austin (USA).

[31] McNeeley, L. A. (1978, January). Thermodynamic properties of aqueous-solutions of lithium bromide. In *ASHRAE JOURNAL-AMERICAN SOCIETY OF HEATING REFRIGERATING AND AIR-CONDITIONING ENGINEERS* (Vol. 20, No. 12, pp. 54-55). 1791 TULLIE CIRCLE NE, ATLANTA, GA 30329: AMER SOC HEAT REFRIG AIR-CONDITIONING ENG INC.

[32] UEMURA, T.; HASABA, S. Studies on the lithium bromide-water absorption refrigerating machine. *Technol. Rep. Kansai Univ*, 1964, vol. 6, p. 31-55.

[33] Poling, B. E., Prausnitz, J. M., & O'connell, J. P. (2001). *The properties of gases and liquids* (Vol. 5). New York: Mcgraw-hill.

[34] J.W. Andberg. Absorption of vapor into liquid films flowing over cooled horizontal tubes. PhD thesis, University of Texas, 1986.

[35] S. V. Patankar. Numerical heat transfer and fluid flow. Hemisphere Publishing Corporation, 1980

[36] Grossman G. Simultaneous heat and mass transfer in film absorption under laminar flow[J]. *International Journal of Heat and Mass Transfer*, 1983, 26(3): 357-31

[37] Bergman T L, Incropera F P. Fundamentals of heat and mass transfer[M]. John Wiley & Sons, 2011.

[38] Touloukian Y S, Ho C Y. Thermophysical Properties of Matter—Specific Heat[J]. *Nonmetallic Solids*, 1649.

[39] McAdams, W. H. (1954). *Heat transmission* (No. 660.28427 M32).

[40] Castro, J., Oliet, C., Rodríguez, I., & Oliva, A. (2009). Comparison of the performance of falling film and bubble absorbers for air-cooled absorption systems. *International Journal of Thermal Sciences*, *48*(7), 1355-1366.

[41] García-Rivera, E., Castro, J., Farnos, J., & Oliva, A. (2016). Numerical and experimental investigation of a vertical LiBr falling film absorber considering wave regimes and in presence of mist flow. *International Journal of Thermal Sciences*, *109*, 342-361.

Annex

The picture below demonstrates the whole setup of the falling film experiment.

Basic energy balance for *Re* as 40, the table below revealed the working data of generator of a typical operation case at the ambient temperature.

Height(m)	Diameter(m)	Surface extension(m^2)	Volume(m^3)
0.5	0.22	0.019	0.3454
T_amb(°C)	λ_la($W \cdot (m \cdot K)^{-1}$)	h_inside ($W \cdot (m \cdot K)^{-2}$)	h_outsideC($W \cdot (m \cdot K)^{-2}$)
25	0.05	94.94	1.53
Re	m_vapor(kg/s)	T_liquid(°C)	
40	1.84E-04	40	

The table below show the leak rate of corresponding component, varies test were made, and the result is the latest test before the formal operation, besides, the leak rate with liquid Nitrogen was calculated under 5 – 30 min due to the fast evaporation process of LN_2 at ambient temperature.

Component	Volume(m^3)	Leak Rate($Pa \cdot m^3 \cdot s^{-1}$)	Leak Rate with LN_2
Tramp	1.60E-04	2.13E-05	6.73E-06
Cylinder	1.90E-02	7.78E-06	5.76E-06
Circle with cylinder	1.90E-02	2.31E-05	8.96E-06
Campana	1.17E-01	9E-05	3.5E-05

The table below shows the working parameter of generator with thermal blanket and isolation material.

Q_abs(W)	T_wall(ºC)	L_La(m)	T_out(ºC)	Q_loss(W)	Q_tot	P_tot	P_out
452.952	53.8	0.05	39.1	14.7	468	1354	3000